National Technical University of Athens
School of Applied Mathematical and Physical Sciences
School of Mechanical Engineering

NCSR "DEMOKRITOS"
Institute of Nuclear and Particle Physics
Institute of Nanoscience and Nanotechnology

Interdepartmental MSc "Physics and Technological Applications"

Measurement of elastic differential cross sections for protons on ^{nat}O in the energy range E= 4-6 MeV, suitable for EBS

MASTER THESIS
of Konstantinos Bosmpotinis

Supervisor: Michael Kokkoris

Athens, July 2022

Acknowledgments

This work is dedicated to my beloved grandma Evdoxaki

Περίληψη

Στην παρούσα εργασία μελετήθηκε η διαφορική ενεργός διατομή της ελαστικής σκέδασης πρωτονίων από φυσικό οξυγόνο, με την σχετική μέθοδο μέτρησης, στο ενεργειακό εύρος $E = 4\text{-}6$ MeV με βήμα 5-15 keV και σε γωνίες ανίχνευσης $\theta = 120^o$ έως 170° με βήμα 10°. Ο λεπτός στόχος που χρησιμοποιήθηκε για το πείραμα, κατασκευάστηκε στο εργαστήριο του ΕΚΕΦΕ ᾽Δημόκριτος᾽ και είχε στο πάνω μέρος του λεπτό στρώμα χρυσού για λόγους προστασίας του στόχου και κανονικοποίησης. Ο καθορισμός της στοιχειομετρίας του έγινε χρησιμοποιώντας πρόσφατα αξιολογημένα δεδομένα διαφορικών ενεργών διατομών. Οι μετρήσεις πραγματοποιήθηκαν με τον επιταχυντή Van de Graaff Tandem 5.5 MV του Εθνικού Κέντρου Ερευνών ᾽Δημόκριτος᾽.

Επιπλέον, πραγματοποιήθηκαν θεωρητικοί υπολογισμοί χρησιμοποιώντας τη θεωρία R-matrix και τον κώδικα AZURE, στο ενεργειακό εύρος $E = 600 - 6000$ keV και σε γωνίες $\theta = 140^o - 170^o$ με βήμα 10°. Τα τελικά αποτελέσματα δείχνουν ικανοποιητική συμφωνία με τα αξιολογημένα δεδομένα, καθώς και με πειραματικά σημεία της παρούσας εργασίας αλλά και με τα δεδομένα από προηγούμενες μετρήσεις που υπάρχουν στην βιβλιογραφία. Τέλος, γίνεται εκτενής σχολιασμός των παρατηρούμενων αποκλίσεων από τη θεωρία, καθώς και για την ανάγκη διεξαγωγής πειραμάτων για αξιολόγηση των πειραματικών και θεωρητικών δεδομένων της παρούσας εργασίας.

Abstract

In this study we present the experimental differential cross sections of $^{nat}O(p, p_0)$ elastic scattering, determined via the relative measurement technique, in the proton beam energy range $E_{lab} = 4 - 6$ MeV with a varying step (from 5-15 keV), at six backscattering detector angles between 120° and 170° (with a 10° step). A thin, self-supporting target manufactured in situ was used in this experiment with a thin layer of gold evaporated on top for wear protection and normalization purposes. The determination of its stoichiometry was carried out according to the currently existing evaluation which has also been benchmarked recently. The measurements were performed using the Van de Graaff Tandem 5.5 MV Accelerator of N.C.S.R. "Demokritos" in Athens, Greece.

In addition, R-matrix calculations for the theoretical investigation of the data have been performed using the publicly available AZURE code in the energy range $E = 600 - 6000$ keV at $\theta = 140^o - 170^o$. The obtained results seem to accurately reproduce the current evaluation, along with the differential cross-section datasets obtained in the present work and already existing ones in literature for this extended proton beam energy range. The observed peculiarities and discrepancies, along with the current needs for validation via accurate benchmarking experiments are discussed and analyzed.

Contents

IX

X

List of Figures

Chapter 1

Introduction

The main goal of this work is the measurement of elastic differential cross sections for protons from oxygen in the energy range E= 4-6 MeV and in backscattering angles $\theta = 120^o, 130^o, 140^o, 150^o, 160^o, 170^o$.

Oxygen has many isotopes, but three of them are stable, namely $^{16}O, ^{17}O$ and ^{18}O with ^{16}O being the most abundant (99.762% in naturally occurring oxygen). It is approximately 21% of the earth atmosphere and comprises about 50% of the earth's crust by mass. Considering that 88.8% of the water mass is oxygen, it is clear that it is present in living organisms in the form of complex compounds, thus playing a key role in a plethora of biological processes. Moreover, it is a highly reactive non- metal which easily forms oxides with other metals and compounds. In particular, oxygen is present in a large variety of materials with industrial, technological and commercial applications. For example, the superconducting properties of high temperature superconductors strongly depend upon their chemical composition. For this reason, it is of paramount importance to know the exact concentration and perform accurate depth profiling measurements of oxygen. Ion Beam Analysis techniques are widely used for thin film depth analysis up to a depth of several micrometers, since they are accurate for depth profile concentration studies and because they are least-destructive. Some of them are briefly discussed in the following paragraphs, with the main focus being on oxygen determination, since their detailed analysis is beyond the scope of this work.

1.1 Nuclear Reaction Analysis

Among all IBA techniques, Nuclear Reaction Analysis (NRA) techniques were first implemented to perform depth profiling of oxygen, since the early sixties [10]. The reactions that are typically studied are listed in Table 1.1 along with their Q-values.

1.1.1 ^{16}O(d, p)^{17}O and ^{16}O(d, a)^{14}N

Deuteron induced reactions are widely used for oxygen depth profiling. Especially the (d, p_0) and (d, p_1) reactions constitute the most popular choices among them because of their positive Q_{value} (there is no energy threshold)

1

and large differential cross sections [18]. These reactions are typically used for energies below 1.1 MeV and provide a powerful tool for near surface layer oxygen detection. In addition, coherent analysis may be achieved by the simultaneous recording of α-particles originating from the $^{16}O(d,_0)$ reaction. As evidenced in IBANDL (Ion Beam Analysis Nuclear Data Library, https://www-nds.iaea.org/exfor/ibandl.htm), all these reactions have been evaluated and partially benchmarked up to $E_{d,lab} = 1.7 - 1.85$ MeV depending on the case. The main advantage of d-NRA is that one can simultaneously detect other light elements that may co-exist in a complex matrix like carbon, nitrogen or boron. However, this may create complications as interference with other peaks in the energy spectrum may occur, like $^{14}N(d, p_5)$, $^{19}F(d, p_{12})$ and $^{11}B(d, p_0)$. The main disadvantage of d-NRA is that it requires low energy deuteron beams, since the (d,n) channel on oxygen opens at 1.829 MeV, thus creating radiation safety issues due to neutron production. Minimal neutron production may also occur from D(d,n) reactions from previously implanted deuterium. At energies above 2.2 MeV (binding energy of deuterons) breakup reactions may also occur, enhancing the neutron production. Therefore, only oxygen concentrations at relatively low depths can be determined. [10].

As mentioned above, (d,a) reactions are also widely used for depth profiling studies in oxygen. Due to their great stopping power, alpha particle beams have high depth resolution, which is useful for thin films depth profiling. As discussed in Ref. [21], (d,a) reactions are preferred over (d, p) for films under 8000Åas they provide a depth resolution in the order of 300Å, as compared to the 2000Åin the (d,p) case.

1.1.2 ^{16}O(^{3}He, p)^{18}F and ^{16}O(^{3}He, a)^{15}O

As mentioned in sec.1.1.1, as the deuteron energy increases, so does the neutron production, since the $^{16}O(d, n)$ reaction is endoergic and has an energy threshold. For this reason, ^3He beams have been quite commonly used for analytical purposes. These beams are advantageous, as they present low neutron yields and provide the possibility to simultaneously perform RBS/EBS and NRA analysis on a sample [3]. Due to the low binding energy (7.7 MeV) of the ^3He particles and the high Q_{value} involved (see Table 1.1), reactions with ^3He beams are mainly exoergic, thus there is a plethora of proton groups that are created, as well as many alphas. They also exhibit a better mass and depth resolution than

Reaction	$Q_{value}(MeV)$
$^{16}O(d, p)^{17}O$	1.918
$^{16}O(d, a)^{14}N$	3.111
$^{16}O(^3He, p)^{18}F$	2.032
$^{16}O(^3He, a)^{15}O$	4.914

Table 1.1: Reactions typically studied in NRA techniques for oxygen depth profiling.

deuterons due to their higher stopping power. However, when there is carbon in the sample to be analyzed, the $^{12}C(^{3}He, p_{0-4})^{14}N$ reaction can interfere with the $^{16}Op_0$ to p_4 groups and contaminate the corresponding peaks. The main issue with ^{3}He beams is that there are no evaluated data available in IBANDL(Ion Beam Analysis Nuclear Data Library), a situation which poses a challenge if accurate oxygen depth profiling needs to be determined. In addition, cross sections involving ^{3}He beams are significantly lower than the corresponding once induced by deuterons or proton beams and the cost of the ^{3}He beam, is considerably higher.

1.2 Rutherford Backscattering

RBS is another nuclear technique for the quantitative analysis of materials. Ion beams (usually protons or alpha particles), are detected in a backscattering geometry to determine the composition of a sample. Since Rutherford cross sections have a Z^2 dependence, this technique is sensitive to heavy elements. However, deviations from the Rutherford cross sections are present at both low and high ion beam energies. As far as low beam energies are concerned, the screening of the nuclear electrostatic potential should be taken into account as discussed in subsection 3.4.2. At higher energies, above the Coulomb barrier, not only the electrostatic potential is responsible for the scattering of the ions, but the nuclear as well. In our case, oxygen is a light element (Z=8), thus deviations from Rutherford occur above 1 MeV for protons and above 2 MeV for alpha particles. Therefore, the RBS technique is not sensitive enough to determine the stoichiometry of oxygen in a heavy matrix, since low oxygen yields are superimposed on a high Z background.

1.3 Elastic Recoil Detection Analysis

Heavy ion beams impinge on a sample with angle a with respect to the normal and the recoiling light nuclei are detected at an angle β using a semiconductor detector, or, in more sophisticated setups, with a magnetic spectro meter or via the time of flight technique. This technique, initially developed to determine hydrogen concentrations in various samples, soon found many applications in quantitative analysis of many light elements, oxygen included. If only light elements are to be detected, it is essential that the ion beam be heavier than the recoiling nuclei. Typically, ^{36}Cl ions are used, having an energy around 30 MeV. Apart from that, ions like ^{63}Cu, ^{127}I and ^{197}Au in the energy range from 2- 200 MeV are also implemented. Assuming that the incident ion is much heavier that the light element to be analyzed, the sensitivity of that method is similar for all the elements (since the recoil cross sections are roughly the same [4]) and it has a Z^4 dependence, where Z is the atomic number of the beam ion.

Overall, ERDA is a powerful tool for the simultaneous detection of many light elements near the surface layer of a sample and offers a great depth

resolution which can reach 10nm. The accuracy of the depth resolution depends on the knowledge of the stopping power of the ion beam inside the target, which in many cases, suffers from many systematic errors and uncertainties. Also, due to the fact that heavy ions are used, beam currents should be kept sufficiently low to avoid target degradation.

1.4   Elastic Backscattering Spectroscopy

Deviations of light element differential cross sections from the Rutherford formula at such low energies can be attributed to their low Coulomb barrier. In these cases, sharp Breit- Wigner resonances occur at certain energies. Moreover, when a ion of several MeV is approaching the vicinity of a target nucleus, nuclear forces are present. Thus, the scattering cross section is a result of an interference between the electrostatic and the nuclear potential and their magnitude cannot be *a priori* calculated theoretically. Therefore, it is crucial that differential cross sections be experimentally measured to calculate light element concentrations and their depth distributions.

Alpha ion beams are commonly used for depth profiling oxygen, since evaluated data for alpha elastic scattering from oxygen are publicly available in the energy range $E_a = 1760 - 6890$ keV at IBANDL, In particular, the 3.04 MeV resonance of the $^{16}O(a,a)$ reaction is widely used to enhance the signal of near surface oxygen in various samples, as shown in Ref. [7]. As mentioned above, alpha particles have an excellent depth resolution due to their high stopping power, as well as superior mass resolution compared to protons and deuterons, but oxygen concentrations studies at higher depths cannot be achieved .

Despite the fact that d-NRA is a well established technique to study oxygen concentrations as described in Sec.1.1, d-EBS has also some interesting applications on oxygen depth profiling, due to its superiority in depth resolution as compared to d-NRA, since outgoing deuterons have lower energies than the corresponding protons or alpha particles emitted from the (d,p) and the (d,a) reactions. Evaluated data available in IBANDL in the energy range $E_{d,lab} = 600-$
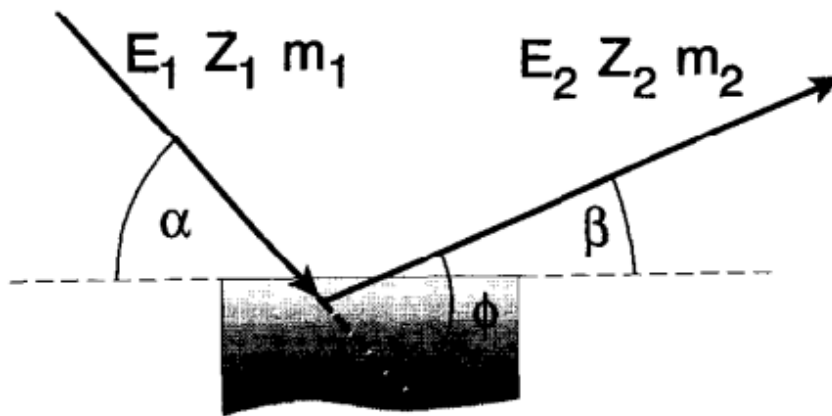
Figure 1.1: Typical ERDA geometry taken from Ref. [4]

1980 keV can be utilized for oxygen depth profiling. Furthermore, cross sections are sufficiently high, thus high sensitivity can be achieved. However, elastic deuteron peak analysis can be impeded if oxygen is present in a high Z- matrix. As a result, d-EBS is usually implemented as a complementary technique along with NRA. Also, RBS techniques can also be employed for the determination of the heavy elements stoichiometry in a martrix.

1.4.1 Proton EBS

In our study the p- EBS technique was implemented to perform oxygen analysis in a disodium phosphate (Na_2HPO_4) target. As mentioned in a previous section, proton elastic scattering starts deviating from the Rutherford formula above 1 MeV. Two narrow Breit- Wigner resonances of the compound nucleus ^{17}F at energies 2.66 and 3.47 MeV have been extensively used to study oxygen concentrations. Proton elastic backscattering cross sections are larger than the corresponding (d,p) and (d,a) ones, leading to a better sensitivity. Hence, great accuracy can be achieved, even if oxygen is in minimal concentrations in a matrix. Also, having lower stopping power, protons are suitable for concentration profiling studies at larger depths. However they lack in depth resolution compared to alpha particles. On the other hand, protons are widely used, because (p,n) reactions usually have a high energy threshold and neutron production is generally maintained at sufficiently low levels. In Table 1.2, common (p,n) reactions have been tabulated. It is clear that due to their high threshold values the (p,n) channel is closed.

Evaluated data of the $^{16}O(p, p_0)$ cross sections are available in IBANDL up to 4 MeV . However, there is an ever growing need to perform depth profiling at larger depths and for this reason it is of paramount importance to increase the proton energy. One additional advantage that accompanies the increase in beam energy , is that the mass resolution improves and peaks from adjacent elements are well separated. Oxygen is usually present in samples along with high-Z elements, a reality that renders the analysis of the corresponding elastically backscattered peaks quite challenging. The advantage of a higher energy proton beam is that Rutherford cross sections drop as E^{-2}, and therefore, the background from high-Z elements is relatively low. Combined with the high cross sections that proton beams offer, p-EBS is an excellent solution for oxygen depth profiling at larger depths.

Reaction	Threshold (keV)
$^{12}C(p, n)^{12}N$	19641
$^{14}N(p, n)^{14}O$	6353
$^{16}O(p, n)^{16}F$	17220
$^{27}Al(p, n)^{27}Si$	5804

Table 1.2: Typical (p,n) reactions and their thresholds .

1.5 Theoretical investigation of the elastic scattering

Before the experiment, a theoretical investigation of the elastic scattering of protons is mandatory. In the energy range studied, namely at E=4-6 MeV per nucleon, the reaction proceeds via the formation of the compound nucleus ^{17}F. The energy levels of the ^{17}F compound nucleus are shown in fig.1.2, along with their corresponding spin- parity assignments.

According to the Q-values, the ^{17}F nucleus can decay in only two particle channels and via photon emission:

$$p +^{16}O \rightarrow^{17} F^* \rightarrow p +^{16}O$$
$$\rightarrow a +^{13}N(Q = -5218.4 keV)$$
$$\rightarrow^{17}F + \gamma$$
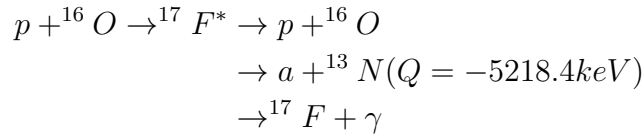
More specifically the $a +^{13}N$ channel is endoergic with a Q-value= -5218.4 keV and a threshold energy of $E_{thres} = 5547.1$ keV.
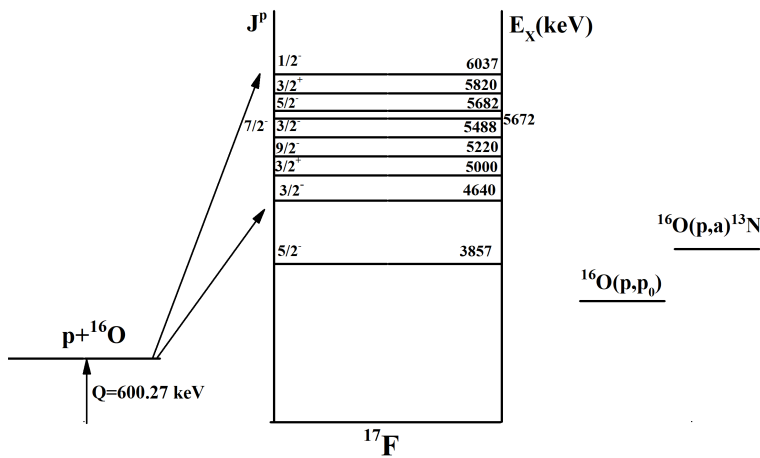
Figure 1.2: Level diagram of the ^{17}F compound nucleus. Energy levels and spin parities were taken from National Nuclear Data Centre website https://www.nndc.bnl.gov/nudat3/getdataset.jsp?nucleus=17F&unc=NDS.

The Q-value for the formation of the compound nucleus is 600.27 keV. So, the energy levels accessible are shown in fig.1.2 within the two arrows. So, we anticipate eight resonances in the excitation function, equal to the number of the accessible energy levels. However, the resonance at $E_x = 5682$ keV is too narrow to be observed ($\Gamma < 0.6$ keV) since the beam energy resolution ~ 1.6 keV. Furthermore, no proton resonance has been observed at $E_x = 5220$ keV.

Chapter 2

Experimental set up

2.1 Tandem Van de Graaff Accelerator at N.C.S.R "Demokritos"

The $^{nat}O(p,p_0)$ differential cross sections were measured using the 5.5 MV Tandem Van de Graaff Accelarator of the Institute of Nuclear and Particle Physics at N.C.S.R. 'Demokritos'. It consists of three basic sectors (see Fig:2.1):

- A sputter source for heavy ion production and an off-axis duoplasmatron source for light ion production. In our study the duoplasmatron ion source was used to produce the protons.

- The tank (Fig: 2.2) which contains the Tandem Van de Graaff Accelerator where ions are accelerated to their maximum energies.

- The analyzing and switching magnets which focus the beam to the reaction chamber and the corresponding beam lines.

The proton beam is produced from the duoplasmatron off-axis source. The emerging negative ions are pre-accelerated entering the pre-acceleration tube at 60 keV. Next, they are attracted by the positive voltage of the Tandem generator and enter the tank, which contains SF_6 gas at high pressure (4.5 bar) for insulation purposes (to inhibit electrical breakdown of the motor rotating the belt). When entering the tank, negative ions pass through a carbon foil of $\sim 10\mu g/cm^2$ where they are stripped from their electrons. Afterwards, the positive ions are repulsed from the positive voltage of the generator and reach their maximum energies. The proton beam, which contains a range of energies, is then guided to the 90° bending analyzing magnet which selects the protons according to their energy by an appropriate magnetic field. A feedback system controls the strength of the magnetic field of the analyzing magnet, which is based on a Nuclear Magnetic Resonance (NMR) probe. The resulting beam has an energy spread around a central value, which is reduced by passing through a system of slits. These slits have typically small widths (≈ 0.3 mm) which is crucial for constraining the energy fluctuation of the beam. Finally, the ion beam enters the switching magnet which directs it towards the desired beam line.

Click on the area of the image map you are interested in.

0. Source and Pre-acceleration Controls (power supplies, misc. electrical units)
1. Sputter Source
2. Duoplasmatron Source
3. Box Lens (powered by common PS)
4. Inflector Magnet
5. Einzel Lens 1
6. Low Energy Slits
7. Low Energy Cup
8. Quartz
9. Low Energy Steerers (4 pairs)
10. Einzel Lens 2
11. Tank
12. In-tank Steerer
13. Charge-stripping Carbon Foil
14. Resistances
15. Hollow Metal Sphere
16. Corona
17. Belt
18. Belt upcharging Power Supply
19. Pulleys
20. Screens
21. High Energy Cup
22. High Energy Quadrupoles (x2)
23. High Energy Steerers (4 pairs)
24. High Energy Slits
25. Analyzing Magnet
26. Analyzer (*iage*) Slits
27. Analyzer Cup
28. Analyzer Quadrupole (x2)
29. Switching Magnet
30. Beamleg Quadrupole

Figure 2.1: Tandem Accelerator at N.C.S.R. 'Demokritos'.[2]
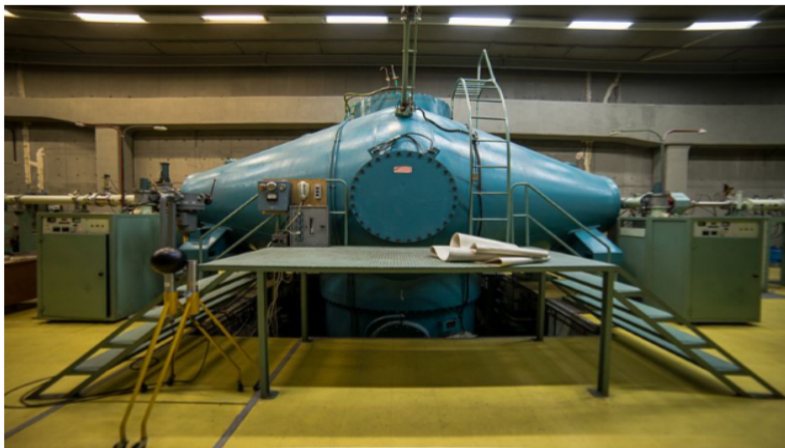
Figure 2.2: The tank of the Tandem Accelerator.

2.2 Experimental details

Protons were accelerated in the energy range E=4-6 MeV with a step of 5-15 keV, entered the reaction chamber, where they impinged on a Na_2HPO_4 target (the stoichiometry of the target will be discussed in Sec.3.4.4). In the middle of the reaction chamber of radius $R \sim 35cm$ the target and six Silicon Surface

Figure 2.4: A cross section of the three layers of the target.

Barrier detectors, used for the detection of the emitted protons, are placed. The target is placed perpendicularly to the beam axis. Small cylindrical tubes were attached on the surface of the SSB detectors to reduce the background from scattered particles on the goniometer walls and the Faraday cup (see Fig: 2.3). During the experiment the whole experimental setup was kept in a vacuum of 10^{-6} Torr, with the use of a combination of rotary and turbo pumps, in order to minimize the collisions of protons with molecules of air, which would result in energy losses and consequently an energy spread of the proton beam. Also, a collimator of 2mm in diameter and an anti-scatterer of 2.5mm in diameter (with a distance of 3cm between them) were placed in the entrance of the chamber, thus constraining the beam size to $\sim 2 - 3mm$ in diameter on the target.
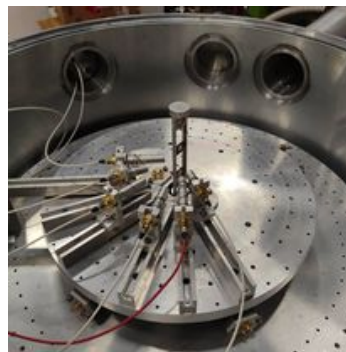
Figure 2.3: All six SSB detectors used in the experiment with the corresponding aluminum tubes.

The target used for the experiment was manufactured at the Institute of Nuclear and Particle Physics of N.C.S.R. 'Democritos'. A thin layer of carbon was evaporated on top of a glass substrate using an electron gun. Afterwards, a thin layer of Na_2HPO_4 was evaporated on top of the carbon foil which served as the backing of the target. Finally, a thin layer of gold was evaporated on top of the Na_2HPO_4 thin layer for wear protection and normalization purposes. It is extremely important that the evaporator be cleaned after the construction of each target layer to avoid cross contamination in future experiments. A schematic of the target is shown in 2.4.

For the detection of protons six Silicon Surface Barrier detectors were placed at $120^o - 170^o$ with a 10° step. The thickness of the detectors was $\sim 500\mu m$,

9

sufficient enough to stop the most energetic protons scattered from the target. Their resolution varied, with the best one being ~ 12 keV and the worst ~ 18 keV. The diameter of each detector was ~ 1cm. A compromise between a desired angular uncertainty and a reasonable counting rate had to be made. In order to keep the angular uncertainty below 1° slits were placed in front of each of the SSB detectors and at the same time to keep counting rate at reasonable levels, the detectors were placed at ~ 10 cm away from the target as shown in fig.2.5.

Figure 2.5: Vertical slits placed to constrain the angular uncertainty.

2.3 Electronics

For the purpose of this experiment standard nuclear instrumentation modules were used which consisted of (per detector):

- A preamplifier which is connected to the detector and its main purpose is an initial amplification of the signal. (5-10 times [19]). Since the detector signal is very weak, the preamplifiers are connected close to it to minimize the electronic noise.

- An amplifier whose main purpose is the amplification of the signal coming from the preamplifier and its shaping in a convenient form for further

processing. A typical amplifier signal is very close to a Gaussian form having the maximum signal to noise ratio.

- An Analog to Digital Converter which converts the analog signal from the analog electronics into a digital form. The time required for the digitization is in the order of a few µs.

- A multichannel Analyzer which records and stores the pulses.
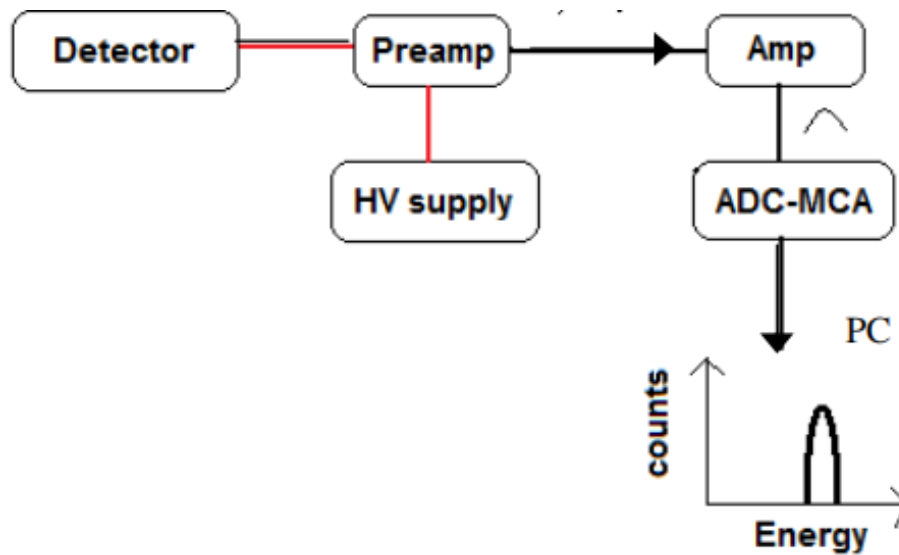
Figure 2.6: Schematic representation of the electronics used to obtain the experimental spectra.

11

Chapter 3

Data analysis

In this chapter, the experimental procedure is described. Emphasis is given in the way the experimental data were collected and analyzed in order to calculate the differential cross sections. All types of error involved in the analysis are also discussed.

3.1 Accelerator Energy Calibration

The energy calibration of the accelerator is an essential part of any nuclear physics experiment for an accurate determination of the differential cross sections. The nominal energy of protons may differ by a few keV from their real energy. As small as it may seem, this difference plays a key role if the structure of the cross section exhibits narrow resonances, where the correct energy assignment is crucial.

The energy of protons is determined by the analyzing magnet by applying a suitable magnetic field. The feedback system which controls the magnetic field of the analyzing magnet is based on a Nuclear Magnetic Resonance (NMR) probe. However, due to remanence and the fact that the NMR probe is not located in the exact center of the magnet, the applied magnetic field may differ from the actual one. As a result, the analyzing magnet does not bend the protons with the desired energy, resulting in the so-called energy offset, which is the difference between the nominal energy and the real one. In addition to that, the proton beam has a Gaussian energy spread around the central value, resulting in the energy ripple, which depends on the opening of the analyzing slits.

The accelerator calibration can be accomplished with various techniques like studying resonances in $^{12}C(p,p_0)$ or by using threshold reactions with neutrons in the exit channel (e.g. $^{7}Li(p,n)^{7}Be$ at 1881 keV). Despite the fact that these techniques accurately determine the energy offset, they suffer at obtaining the ripple of the beam with high precision. For the purposes of this experiment, the study of the $^{27}Al(p,\gamma)$ reaction has been selected for the accelerator calibration. The $^{27}Al(p,\gamma)$ reaction exhibits a narrow resonance of $\Gamma = (110 \pm 20)$ eV at the proton lab energy $E_{p,lab} = (991.89 \pm 0.11)$ keV . The reaction Q-value is 11584.9 keV. The gamma- ray of $E_\gamma = 1779$ keV from the first excited state to the ground state of the compound nucleus ^{28}Si (see Fig:3.1) is detected by a germanium detector. Protons impinged on a thick aluminum target placed in

front of the faraday cup, at the end of the beam line and the resulting gamma-rays were detected by a HPGe detector. The proton energy varied from 980 keV to 1010 keV. More specifically, proton energy step was 1 keV or 2 keV in the energy range $E = 990 - 1005$ keV to properly scan the resonance. In the end, we collected 19 different spectra, one for each energy used. In the obtained gamma-ray spectrum the photopeak at 1779 keV was identified and integrated using the TV software [20]. The total counts of the peak were normalized over the total charge, thus obtaining the normalized yield. Then, the normalized yield of the photopeak of interest for each energy is plotted (see Fig: 3.2) with respect to the proton lab energy. Data were were fitted using a sigmoidal function of the form

$$f(x) = a + \frac{a - b}{1 + e^{\frac{x - x_0}{c}}} \tag{3.1}$$

Where a, b, c, x_0 are the parameters to be determined from the fitting of the data. More specifically a refers to the lower plateau of the curve, b is the upper one and x_0 is the energy at the mid-point of the sigmoidal rise which corresponded to 991.85 keV. The energy offset is determined at the mid-point of the sigmoidal rise, therefore the offset was found to be equal to ~ 0.04 keV. The lower and upper limits of the ripple occur at the 11% and 88% of the sigmoidal rise:

$$y_{lower} = a + (b - a) \times 11\%$$
$$y_{upper} = a + (b - a) \times 88\%$$

and the corresponding energy ripple was found to be equal to ~ 1.6 keV.
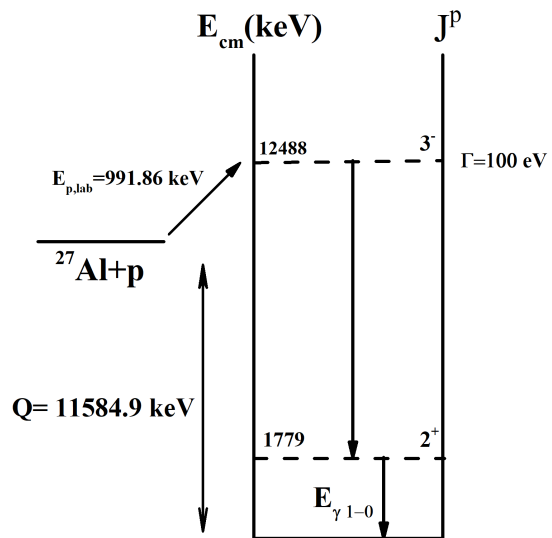
Figure 3.1: A reduced level diagram of the compound nucleus ^{28}Si.
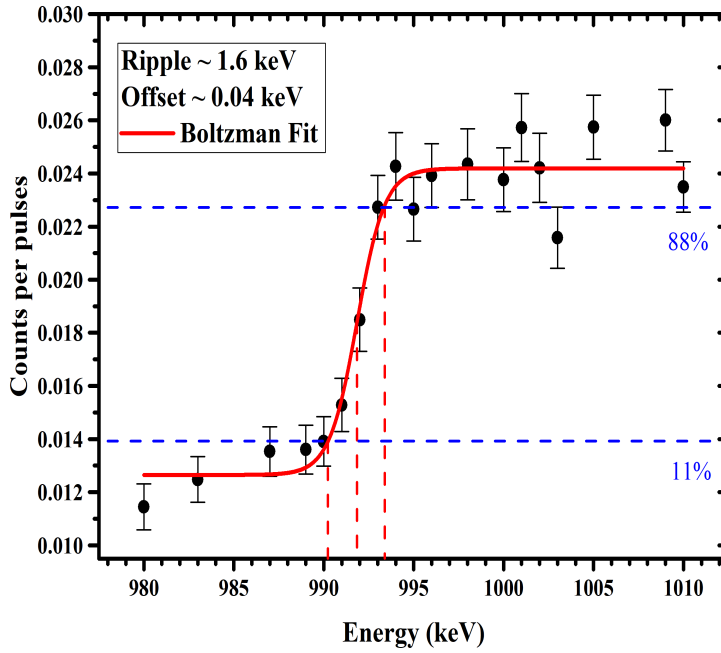
Figure 3.2: Sigmoidal function fit to the experimental points to calculate energy offset and ripple.

Finally, the real energy of the proton beam is given by:

$$E_{beam} = (E_{nom} + offset) \pm ripple \qquad (3.2)$$

3.2 Energy loss and energy straggling calculations at half the target thickness

It is well known that charged particles lose energy as they pass through a material. The amount of energy loss per traversed distance depends on the projectile- target combination, the density and composition of the target as well as the incident ion energy. In our study, a proper energy correction had to be carried out to account for those losses, since interactions do not take place only on the surface of the target, where the energy loss is negligible. Since interactions can occur in any layer of the target (and thus in different energies), we assume that protons interact with oxygen at its mean thickness inside the target. Following the energy calibration of the accelerator, the differential cross sections were attributed to the energy:

$$E_{final} = E_{beam} - \Delta E_{Au} - \Delta E_{O/2} \qquad (3.3)$$

where E_{beam} is the proton beam energy after the accelerator energy calibration, ΔE_{Au} is the energy loss in the surface layer of gold and $\Delta E_{O/2}$ is the energy loss till the half target thickness of oxygen inside the target. The proton beam

16

energy losses were calculated via the SIMNRA code. The Ziegler/ Biersack [6] stopping power model has been used and it was found that the proton beam loses ~ 5 keV in the middle of the target for beam energies between $E = 4$ MeV to 5.3 MeV and 4 keV for beam energies $E = 5.3$ MeV to 6 MeV. The energy straggling has been computed using Chu [9] and Yang [24] model incorporated in the SIMNRA code and it was found to be approximately equal to 5.6 keV. The total error in the energy was ~ 6 keV and was determined by the quadratic sum of the energy ripple and energy straggling:

$$\delta E_{final} = \sqrt{E_{ripple}{}^2 + E_{straggling}^2} \tag{3.4}$$

3.3 Analog to Digital Converter calibration

The final data that need to be analyzed are shown in a spectrum(see 3.4). In the vertical axis there are the total counts, while in the horizontal axis lie the corresponding channels. The calibration of each ADC was achieved using the thin surface layer of gold evaporated on top of the target. The energy of the elastically scattered protons can be calculated using basic kinematics (conservation of energy and momentum). Protons scattered from gold at angle θ had a specific energy which could then be matched with the corresponding peak channel. This energy can be calculated analytically using the kinematic factor, via the equation:

$$K = \frac{E_1}{E_0} = \left[\frac{M_1 \cos\theta + \sqrt{M_2^2 - M_1^2 \sin^2\theta}}{M_1 + M_2} \right]^2 \tag{3.5}$$

where K is the kinematic factor, E_0 is the proton beam energy after the accelerator energy calibration, E_1 the energy of the scattered protons at angle θ and M_1, M_2 the atomic masses of proton and gold respectively. The CATKIN software [8] was used for such calculations. Since the layer of gold was ultra thin, the corresponding channel was the gold signal peak. After the channels and the energies were determined, the data were plotted on a graph, where on the horizontal axis is the channel number and on the vertical axis is the energy of backscattered protons from gold. The relation between the energies of the scattered protons and the corresponding channel is linear of the form $E = aC + b$. Therefore, when a linear fit is performed to obtain the gain a in keV/ch and the offset b in keV, the conversion of a backscattering spectrum from channel numbers to particle energies is achieved. In fig:3.3 the calibration of the ADC for the backscattering angle $\theta = 170^o$ at the last day of the experiment is shown in the energy range $E = 1010 - 5545$ keV, resulting in a gain $a \sim 4.22$ keV/ch and an offset $b \sim 39$ keV. Finally, the obtained R-factor of the fitting procedure was almost equal to one, something which confirms the excellent linearity of the ADC.
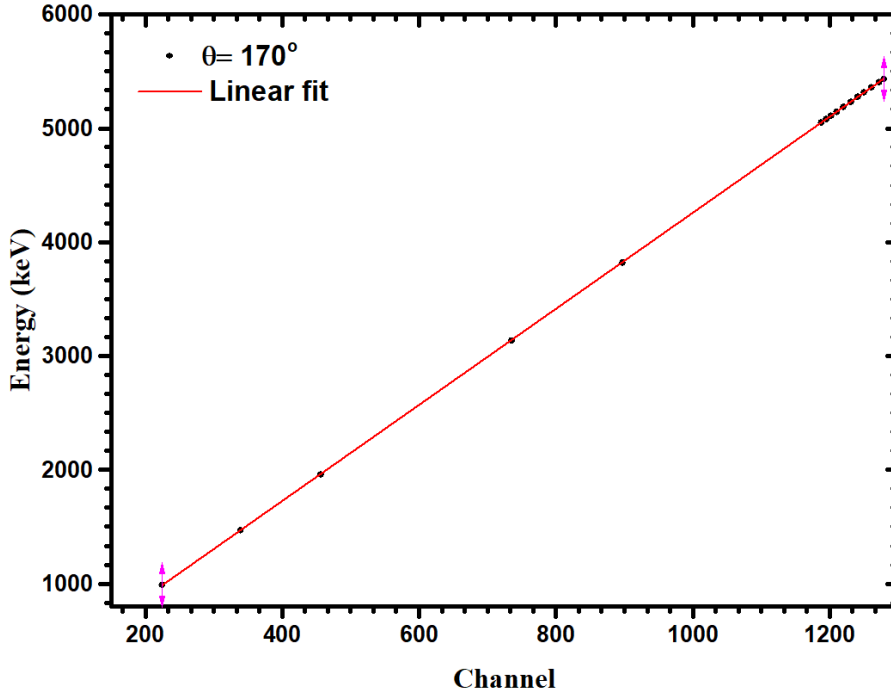
Figure 3.3: Calibration curve of the ADC at $\theta = 170^o$.

3.4   Differential cross section determination

3.4.1   Relative measurement technique

The experimental differential cross section values for the elastic back-scattering of protons from a light element can be calculated using the absolute measurement technique via the equation:

$$\left(\frac{d\sigma}{d\Omega}\right)_{E,\theta} = \frac{Y}{\epsilon \cdot Q \cdot \Omega \cdot N} \tag{3.6}$$

where

- Y is the number of protons scattered from the light element.

- ϵ is the efficiency of the detector, which in our case is equal to one.

- Q is the total charge that hit the target in each measurement. So, it corresponds to the total number of protons that impinge on the target.

- Ω (in sr) is the detector solid angle placed at angle θ.

- N is the element target thickness in areal density units (atoms/cm^2).

Note that E refers to the energy of the protons at half of the target thickness. However, in our study ,the absolute technique for calculating differential cross sections was not the preferred one, because there are several sources of error in the determination of the solid angle of the detector and the total corresponding

18

charge in the target. The total charge is the sum of the charge from the Faraday cup and the charge induced in the target. However, when protons hit the target secondary electrons and photons are emitted. In many cases electron currents can be comparable to or even higher than the beam current, depending on the beam- target combination. The solid angle determination can be performed using an accurately calibrated alpha particle source, emitting alphas at 4π. However, systematic errors occur due to the difference in dimensions of the source and the beam spot and the difficulty of mounting the source in the exact same place of the target. So, the product $Q \cdot \Omega$ has a large uncertainty due to the afore mentioned problems regarding the accurate charge collection and the accurate detector solid angle determination. To overcome this, the relative measurement technique was implemented to calculate the differential cross sections. Gold is a heavy element which strictly follows Rutherford cross section in the energy range studied. So, experimental differential cross sections of oxygen and gold are given by:

$$\left(\frac{d\sigma}{d\Omega}\right)^{^{16}O}_{E,\theta} = \frac{Y_{^{16}O}}{\epsilon \cdot Q \cdot \Omega \cdot N_{^{16}O}} \tag{3.7}$$

$$\left(\frac{d\sigma}{d\Omega}\right)^{Au}_{E',\theta} = \frac{Y_{Au}}{\epsilon \cdot Q' \cdot \Omega' \cdot N_{Au}} \tag{3.8}$$

In our case, gold and oxygen are present in the same target, thus for each measurement the total charge impinging on it and the solid angles for each element are equal($Q = Q', \omega = \omega'$). So, dividing both sides of 3.7 and 3.8, the terms $Q \cdot \Omega$ are cancelled out and the experimental differential cross sections of oxygen are given by:

$$\left(\frac{d\sigma}{d\Omega}\right)^{^{16}O}_{E',\theta} = \left(\frac{d\sigma}{d\Omega}\right)^{Au}_{E,\theta} \cdot \left(\frac{Y_{^{16}O}}{Y_{Au}}\right) \cdot \left(\frac{N_{Au}}{N_{^{16}O}}\right) \tag{3.9}$$

Therefore the accuracy in the calculation of the differential cross sections of elastic scattering of protons from oxygen depends on the accurate determination of the three factors that appear in eq. 3.9. The differential cross section for oxygen is calculated on the energy E', taking into account the energy loss of the beam inside the target (see 3.2). The energy E, is defined as the beam energy after the accelerator energy calibration.

3.4.2 Rutherford differential cross sections of gold

The first term in 3.9 is nothing more than the Rutherford cross section formula. Since, differential cross sections are calculated in the laboratory frame, Rutherford formula in lab frame takes the form:

$$\left(\frac{d\sigma_R}{d\Omega}\right)_{E,\theta} = \left(\frac{Z_1 Z_2 e^2}{4E}\right) \cdot \left(\frac{2\left[\left(M_2^2 - M_1^2 \sin^2\theta\right)^{1/2} + M_2\cos\theta\right]^2}{M_2\sin^4\theta\left(M_2^2 - M_1^2\sin^2\theta\right)^{1/2}}\right) \tag{3.10}$$

In our case $M_1 = 1.007825 amu, M_2 = 196.96657 amu$ are the proton and gold masses respectively and $Z_1 = 1, Z_2 = 79$ are the atomic number of protons and gold respectively. So, eq.3.10 describes the scattering of protons of energy E from gold nuclei at scattering angles θ in the lab frame. Equation 3.10 is valid for protons in the energy range 4-6 MeV, because gold has a large atomic number, thus having great Coulomb barrier. However, due to screening effects, protons do not interact with the total charge of the gold nuclei. This effect, can result in certain deviations from the Rutherford formula. In fact, screening effects take place for every projectile- target combination, but as the target atomic number increases, K-shell electrons are closer to the nuclei, thus resulting in a much more screened electrostatic potential. Therefore, to account for these effects, eq.3.10 had to be multiplied with a correction factor, namely L´ Ecuyer factor, given by [16]:

$$F_{L' \text{ Ecuyer}} = 1 - \frac{0.4873 \cdot Z_1 \cdot Z_2^{4/3}}{E_{cm}} \tag{3.11}$$

Where E_{cm} is the energy in the center of mass. It is obvious, from eq. 3.11 that L' Ecuyer correction factor becomes smaller as the projectile energy increases. The final expression to calculate the Rutherford corrected cross sections for each energy and angle is given by:

$$\left(\frac{d\sigma}{d\Omega} \right)_{E,\theta}^{Au} = F_{L' \text{ Ecuyer}} \cdot \left(\frac{d\sigma_R}{d\Omega} \right)_{E,\theta}^{Au} \tag{3.12}$$

We assign no statistical or systematic error to this term, since this is a standard, generally accepted analytical computation.

3.4.3 Spectrum peaks integration

To calculate the second term in 3.9 the counts in each peak in the spectrum should be known. More specifically, the Tv spectroscopy code [20] was used to integrate the peaks of oxygen and gold in each energy for all six backscattering angles.

A typical spectrum at the proton lab energy of $E = 5050$ keV for $\theta = 120^o$ is shown in fig:3.4. It is clear that there are also peaks in our analysis that originate from the elastic scattering of protons from other elements that are present in the target. After the calibration of the ADCs, the oxygen peak can be easily identified by basic kinematics. As it can been seen from fig:3.4 apart from the oxygen and gold peaks which were identified and integrated to calculate the total counts, there are also the elastic backscattered peaks of protons from ^{12}C and its second most abundant isotope of ^{13}C, as well as from ^{14}N which appeared as a contaminant from the manufacturing of the target and finally from ^{23}Na and ^{31}P that were present in the chemical composition of the target.

A linear background was assumed to integrate the peaks of gold and oxygen. In both cases, counts were described by a Gaussian distribution. So, the statistical error of the under-study peaks is given by the square root of total counts ($\sqrt{N}$). To keep the statistical errors below 2%, a sufficient number of

counts in each of the under study peaks had to be collected. Systematic errors arising from the determination of the background base line did not exceed 2% in all cases.
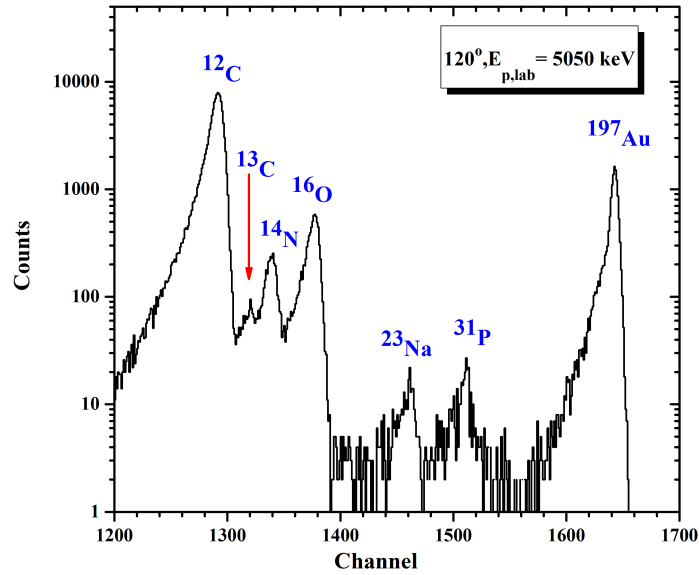
Figure 3.4: A typical spectrum for the proton lab energy of 5050 keV and for $\theta = 120^o$ shown in logarithmic scale. The elastic backscattering peaks of protons from all the elements/isotopes in the target have also been identified.

3.4.4 Target characterization

The most challenging factor for the accurate determination of the differential cross section, is the calculation of the N_{au}/N_O ratio. Initially, measurements were taken at proton beam energies $E = 2000, 2300, 3200$ and 3900 keV at angles $140^o - 170^o$ with a 10° step.

The resulting twenty experimental spectra were simulated using the SIMNRA code [17]. To calculate the N_{au}/N_O ratio for each spectrum a set of parameters had to be determined. Firstly, a target with the appropriate number of layers, elements and stoichiometry had to be prepared which best described the actual composition of the target, along with the type of the incident beam, the energy, the energy spread and the scattering angle of the protons. Additional input parameters were the detector resolution, the calibration offset (keV) and gain (keV/channel) of each of the ADCs and the selection of the evaluated data from SigmaCalc library for each element and reaction in the spectrum. Afterwards, a double fitting of the product $Q \cdot \Omega$ of the total accumulated charge in the target with the solid angle of each detector, along with the thickness of the gold surface layer had to be performed. To achieve this, Rutherford cross section data sets were utilized for gold. SIMNRA code features L'Ecuyer screening corrections for more accurate differential cross section calculations. In addition, SIMNRA also includes Andersen corrections but there were no significant differences between the two models. Subsequently, the gold layer thickness was kept constant for all the proton lab energies and scattering angles and by varying the product
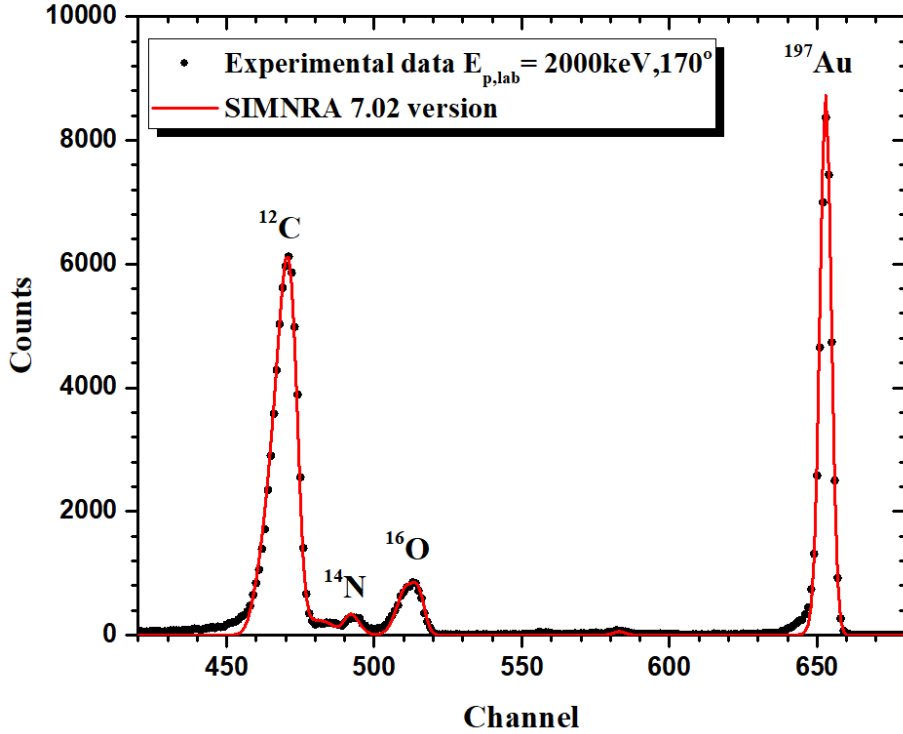
Figure 3.5: Typical experimental and simulated spectrum using SIMNRA code at proton lab energy $E = 2000$ keV and $\theta = 170^o$.

$Q \cdot \Omega$ the remaining gold peaks were fitted. After that, the areal density of oxygen in the target can be calculated by varying its composition in each target layer. The total number of counts in the experimental and simulated spectra for both oxygen and gold peaks had to be matched. Evaluated data available in IBANDL for proton elastic backscattering from carbon, oxygen, nitrogen and phosphorous were used to simulate each peak whenever these data were available. The proton energies for target thickness measurements were carefully selected to be far from the two existing Breit-Wigner resonances at $E_p = 2663$ keV and at $E_p = 3470$ keV to maximize the accuracy. Finally, for each energy and angle a unique N_{Au}/N_O ratio has been calculated and in the end, the average of these twenty measurements was adopted and the corresponding ratio was found to be $N_{Au}/N_O \sim 0.210 \pm 0.007$

Target thickness measurements were also performed during the third day of the experiment at beam energies $E = 2, 3.2, 3.9$ MeV and at angles $\theta = 140^o - 170^o$ to check for target degradation and cross validate with the initial measurements. However, the average of those twelve measurements, which was calculated with the same procedure as discussed above, was found to be $N_{Au}/N_O = 0.295 \pm 0.019$. This corresponds to a discrepancy of 40% between the first and the last day that could be attributed to the fact that the third day of the experiment, sharp changes in the beam energy were made, namely from 6 MeV down to 5.5 MeV and then from 5.14 MeV down to 3.9 MeV, where the target thickness measurements were performed. This could potentially move the beam spot and due to target lateral inhomogeneities, the target profile changed. So, in order to check whether

these changes took place during the course of the experiment, we duplicated our measurements at $E = 4.9$ MeV for day one to day two of the experiment, for the detectors at angles $\theta = 120^o - 160^o$. Given the fact that the proton beam energy remained the same between these two days, so do the differential cross sections for oxygen $(d\sigma/d\Omega)_O^{(1)} = (d\sigma/d\Omega)_O^{(2)}$ and gold $(d\sigma/d\Omega)_{Au}^{(1)} = (d\sigma/d\Omega)_{Au}^{(2)}$ for a given angle. Therefore, a relation between the ratio of the experimental yields of oxygen and gold of two days with the ratio of the corresponding target thickness can be deduced:

$$\frac{\left(\dfrac{Y_O}{Y_{Au}}\right)^{(1)}}{\left(\dfrac{Y_O}{Y_{Au}}\right)^{(2)}} = \frac{\left(\dfrac{N_{Au}}{N_O}\right)^{(2)}}{\left(\dfrac{N_{Au}}{N_O}\right)^{(1)}} \tag{3.13}$$

Comparing the yields of oxygen and gold between the two days, one can compute the difference between the N_{Au}/N_O ratio. So, a decrease of of 3.5% was noticed in the N_{Au}/N_O ratio between day one and day two of the experiment. We also duplicated our measurements in the energy range $E = 5140 - 5545$ keV for the detectors at $\theta = 140^o - 160^o$. An increase of 2% in the N_{Au}/N_O ratio was found between day two and day three along with an energy shift of 3 keV in the proton lab energy. Therefore, no significant differences in the target profile (N_{Au}/N_O ratio) were found during the measurements of the differential cross sections and so, the beam spot must have moved by a few mm during the transition from 5140 keV to 3900 keV (where the target thickness measurements took place), which means that no experimental data point had to be rejected, apart from the target thickness measurements on the third day of the experiment.

Finally, due to the possible sensitivity of the target thickness ratio when performing large energy shifts, only the measurements at $E = 3.9$ MeV were considered for the calculation of the gold to oxygen ratio. Thus, the final result along with the statistical error was 0.220 ± 0.004 and this one was used to calculate the experimental cross sections along with the aforementioned corrections of 3.5% from day one to day two and 2% from day two to day three.

$\theta(deg)$	$N_{Au}(10^{15}atoms/cm^2)$	$N_O(10^{15}atoms/cm^2)$	N_{Au}/N_O
140	85.4	397.5	0.2148
150	85.4	390.5	0.2187
160	85.4	387.7	0.2203
170	85.4	379	0.2253

Table 3.1
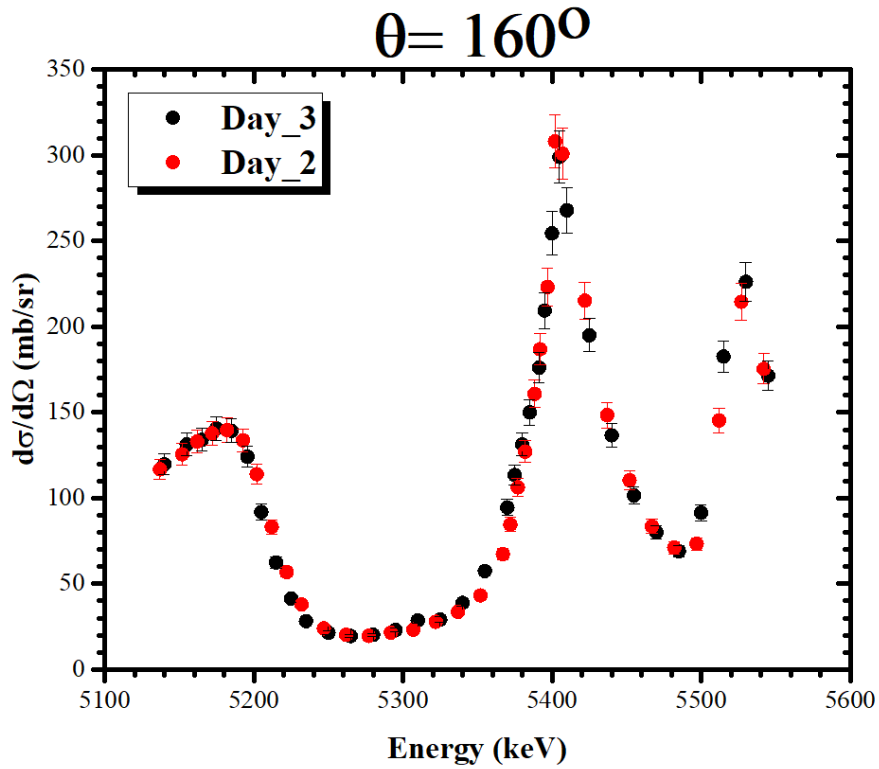
Figure 3.6: Differential cross sections comparison between day two and day three of the experiment for the detector at $\theta = 160^o$. The correction of 2% along with the 3 keV energy shift in proton beam energy is shown. A satisfactory matching is achieved when these corrections are applied, especially at the peak of the narrow resonance at $E_{p,lab} = 5405$ keV.

Chapter 4

Results

4.1 Differential cross sections results

In this chapter, the final results of the elastic backscattering differential cross sections of protons from ^{nat}O at angles $\theta = 120^o - 170^o$ with 10° step in the energy range E=4-6 MeV are presented. The energy step varied from 5-15 keV to probe the structure of narrow resonances of the compound nucleus ^{17}F. The resulting cross sections are tabulated in 4.1 for the angles $\theta = 120^o - 160^o$ and in 4.2 for the detector at $\theta = 170^o$, along with the corresponding statistical errors, which make less than 5% of the differential cross sections measured. Statistical errors arise from the integration of the peaks of gold and oxygen, as well as, from the measurement of the target thickness. A 5% systematic error assigned to the gold to oxygen ratio $N_{Au}/N_{^{16}O}$ arises from uncertainties pertinent to the stopping power model used in the SIMNRA code and due to lateral inhomogeneities of the target. Propagating the statistical errors, a final expression for the statistical error at each energy step is given by the quadratic sum of each term:

$$\delta \left(\frac{d\sigma}{d\Omega} \right) = \frac{d\sigma}{d\Omega} \cdot \sqrt{ \left(\frac{\delta Y_{^{16}O}}{Y_{^{16}O}} \right)^2 + \left(\frac{\delta Y_{Au}}{Y_{Au}} \right)^2 + \left(\frac{\delta \left(\frac{N_{Au}}{N_{^{16}O}} \right)}{\left(\frac{N_{Au}}{N_{^{16}O}} \right)} \right)^2 } \qquad (4.1)$$

The accelerator energy calibration was performed at the last day of the experiment. The offset was found to be 0.04 keV, which means that the nominal energy matched the real energy at day three. As stated in sec.3.4.4 proton energies had an offset of 3 keV on day one and day two, which means that this extra offset had to be subtracted from the nominal energy, except for the measurements for the detector at $\theta = 170^o$ in the energy range E=5140- 5545 keV.

In figures 4.2-4.7 the differential cross sections are plotted in logarithmic scale with respect to the proton laboratory energy, calculated at half the oxygen layer thickness inside the target. Error bars in the horizontal axis (energy) are not visible due to the adopted graph scale. Rutherford cross sections are also plotted in the same graph, along with the corresponding screening correction for oxygen for direct comparison. The experimental differential cross sections

are systematically higher for all the energies at all six backscattered angles from Rutherford cross sections by a factor raging from 4 to 138 at certain resonances and angles . This is not surprising since oxygen is a light element and thus, strong deviations from the Rutherford cross section values are anticipated even at 1 MeV proton lab energy. Also, the Rutherford formula predicts that differential cross sections follow the $1/E^2$ law with respect to the beam energy , something which clearly fails to interpret the six Breit-Wigner resonances in the cross section structure, which originate from the energy levels of the compound nucleus ^{17}F.

In figures 4.8-4.13 differential cross sections of the present work are plotted in the same graph along with the ones determined by Harris et al.[12] and Jarmie et al[14]. The cross section is dominated by the broad resonance of the ^{17}F compound nucleus at $E_x = 5$ MeV, $J^\pi = 3/2^+$. This state is formed by p-wave protons and has a width $\Gamma = 1530$ keV, which means that possible interferences of it with neighboring resonances, can strongly affect their shape and amplitude. Another thing to consider is the strong angular distribution of the resonances at $E_{p,lab} = 4.294$ MeV and 5.195MeV which can be attributed to the energy levels of the ^{17}F compound nucleus at $E_x = 4640$ keV ($\Gamma = 225$ keV) and $E_x = 5488$ keV ($\Gamma = 68$ keV) respectively, with total spin- parity $J^\pi = 3/2^-$ (also formed by p-wave protons). In particular, their interference with the broad resonance at $E_x = 5000$ keV is destructive at the more backward angles $150^o - 170^o$ and constructive at the forward scattering angles $120^o - 140^o$. Also, the structure of the resonances of ^{17}F at $E_x = 5672$ keV ($\Gamma = 40$) (only f- wave protons form this state) and $E_x = 6037$ keV ($\Gamma = 30$) keV respectively is visible. Moreover, in the high energy region (E= 5850- 6000 keV) as shown in 4.1, the angular distribution of the cross section is weak. Also, the differential cross section varies smoothly with the energy and at the same time its value is $\sim 20mb/sr$. This high energy region can be particularly useful for oxygen depth profiling in larger depths for two reasons. Firstly, the cross section sensitivity remains at satisfactory levels and secondly, it could be advantageous for experimental setups when the beam energy or scattering angle are not well known with high accuracy.

The measurements of the present work agree with the current evaluation within 10% in the energy range $E = 4000 - 4080$keV which can be justified by the systematic errors due to the the stopping power model and the lateral inhomegeinities of the target and the statistical errors involved in the measurem ents. However, an underestimation of the measured differential cross section with the current evaluation up to 18% is observed at $\theta = 120^o$. In this geometry the resulting peaks are broader (with a pronounced left asymmetry). Thus, it is possible that the neighboring peak of nitrogen overlaps with that of oxygen, thus posing a challenge concerning the limits of integration.

Measurements of the elastic backscattering cross sections of protons from oxygen have been measured by Harris et al up to 5.63 MeV for the scattering angles $122, 3^o, 128, 6^o, 138.4^o, 147.5^o, 160.1^o$ and 165.9^o. Comparing these measurem ents with the ones of the present work, it is clear that the present cross sections are systematically lower up to 35% in the proton lab energy range $E_{p,lab} = 4000 - 5100$ keV for the detection angles $\theta = 120^o, 130^o$, in the energy range

$E_{p,lab} = 4000 - 5350$ keV for the detection angles $\theta = 140^o, 150^o$ and in the energy range $E_{p,lab} = 4400 - 5100$ keV for the detection angles $\theta = 160^o, 170^o$. Also, notable discrepancies between Harris et al and the results of the present work are observed at the maximum of the yield at $E_{p,lab} = 5400$ keV for the detection angles $\theta = 120^o - 150^o$ raging from 20%- 28%. On the other hand, the two datasets show a remarkable agreement in the energy range $E_{p,lab} = 4000 - 4400$ keV for the detection angles $\theta = 160^o$ and 170°. Energy shifts of 22keV, 50keV, 45keV between the two datasets are also observed at the detection angles $\theta = 120^o, 130^o$ and 150° respectively. The reasons for these discrepancies are not clear, but it should be noted here that in the work of Harris et al. a gas target was used, while the $^{11}B(p, a_0)$ reaction was implemented for the accelerator energy calibration, yielding a stated error of ± 20 keV in the determination of the proton beam energy, a method generally considered inferior to the implementation of sharp, narrow gamma-ray resonances, adopted in the present work. As far as Jarmie et al is concerned, there is an excellent agreement with the results of the present work up to 4400 keV, with increasing deviations at higher energies.
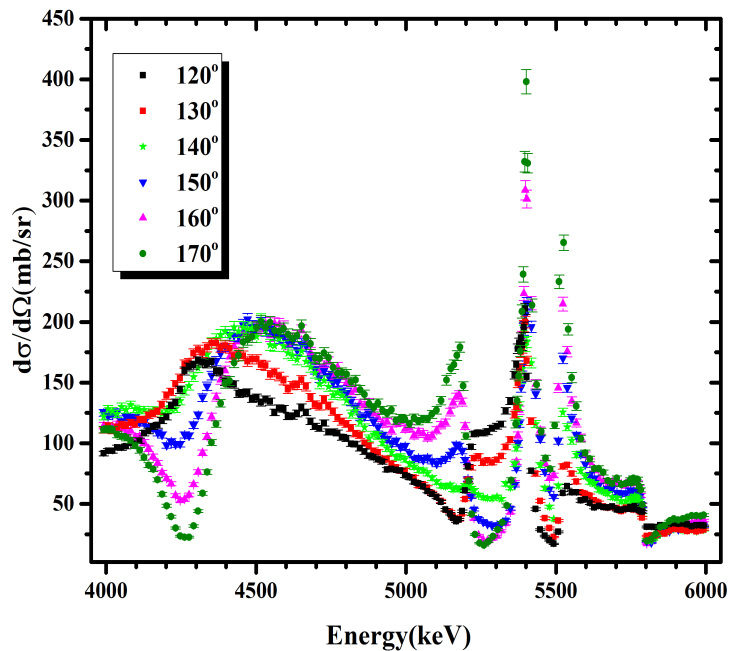
Figure 4.1: The experimental cross sections for the angles $\theta = 120^o - 170^o$ plotted in one graph. The angular dependence of the differential cross sections near the resonances of the compound nucleus is evident.
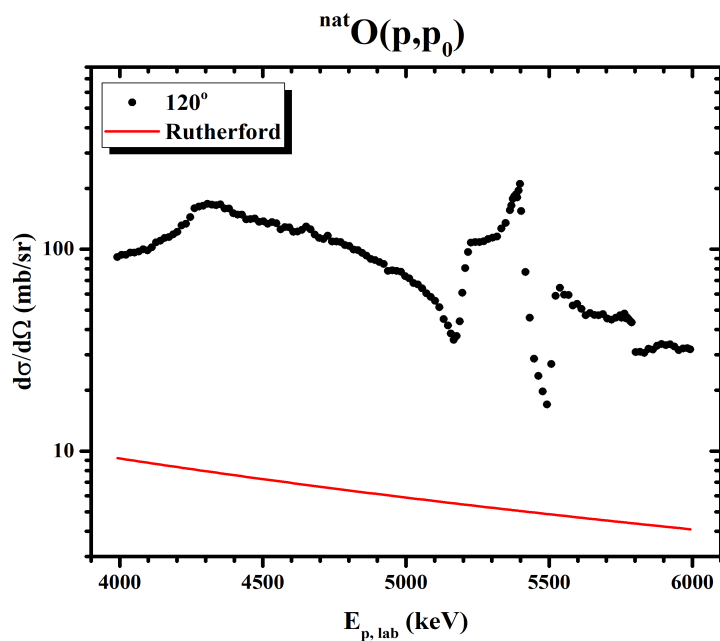
Figure 4.2: Experimental differential cross sections of the elastic backscattering of protons from ^{nat}O of the present work (black dots) along with the Rutherford formula cross section values (solid red line) for the detection angle $\theta = 120^o$ plotted in logarithmic scale.
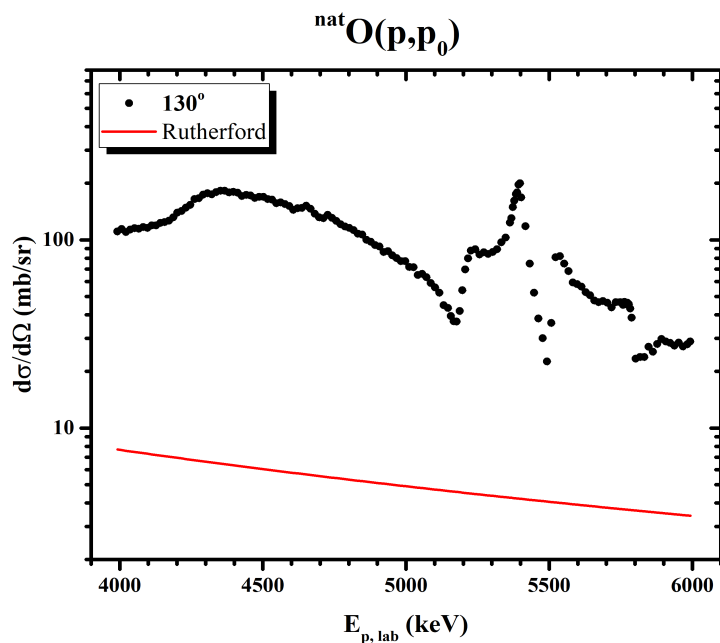
Figure 4.3: Experimental differential cross sections of the elastic backscattering of protons from ^{nat}O of the present work (black dots) along with the Rutherford formula cross section values (solid red line) for the detection angle $\theta = 130^o$ plotted in logarithmic scale.
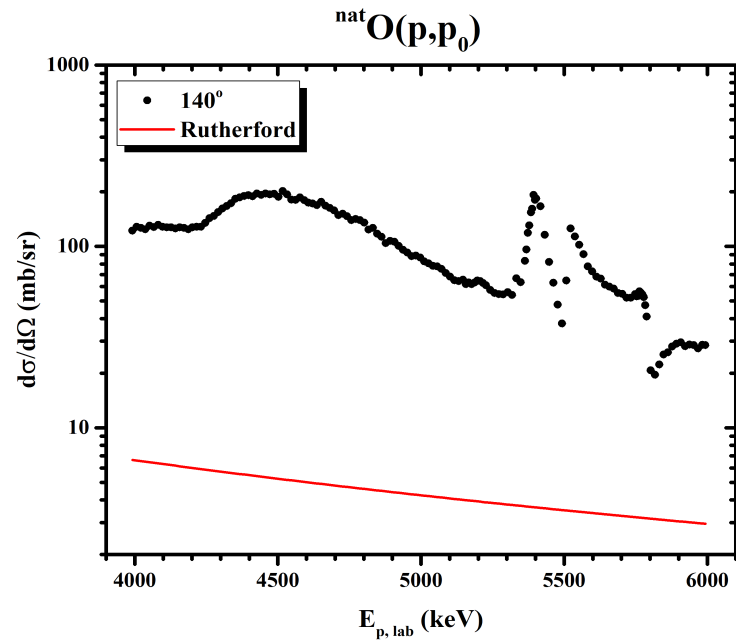
Figure 4.4: Experimental differential cross sections of the elastic backscattering of protons from ^{nat}O of the present work (black dots) along with the Rutherford formula cross section values (solid red line) for the detection angle $\theta = 140^o$ plotted in logarithmic scale.
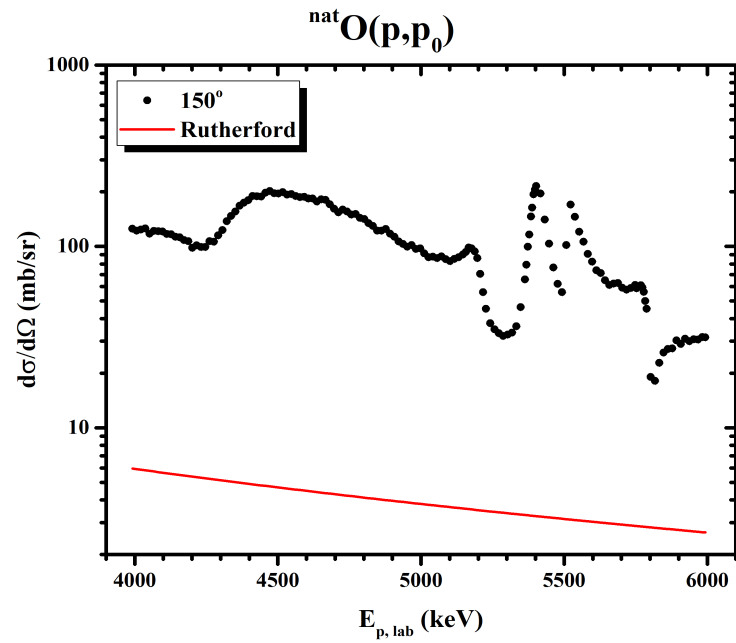
Figure 4.5: Experimental differential cross sections of the elastic backscattering of protons from ^{nat}O of the present work (black dots) along with the Rutherford formula cross section values (solid red line) for the detection angle $\theta = 150^o$ plotted in logarithmic scale.
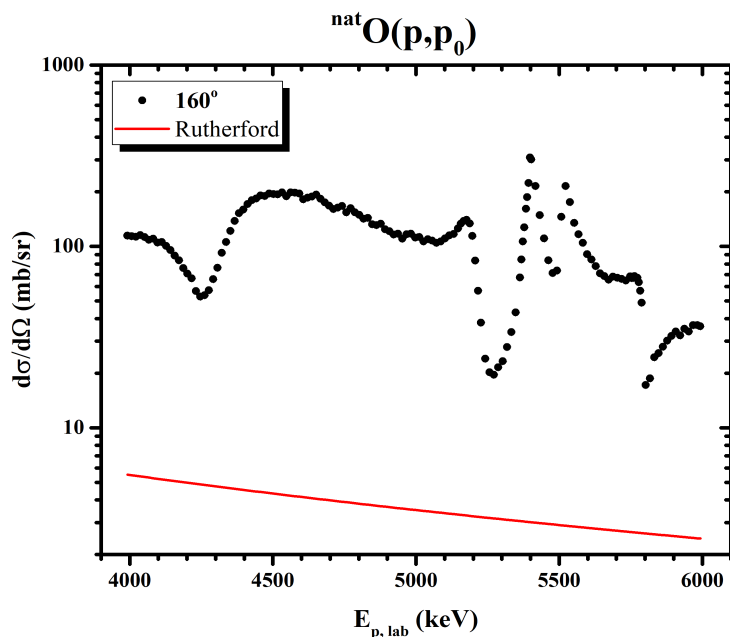
Figure 4.6: Experimental differential cross sections of the elastic backscattering of protons from ^{nat}O of the present work (black dots) along with the Rutherford formula cross section values (solid red line) for the detection angle $\theta = 160^o$ plotted in logarithmic scale.
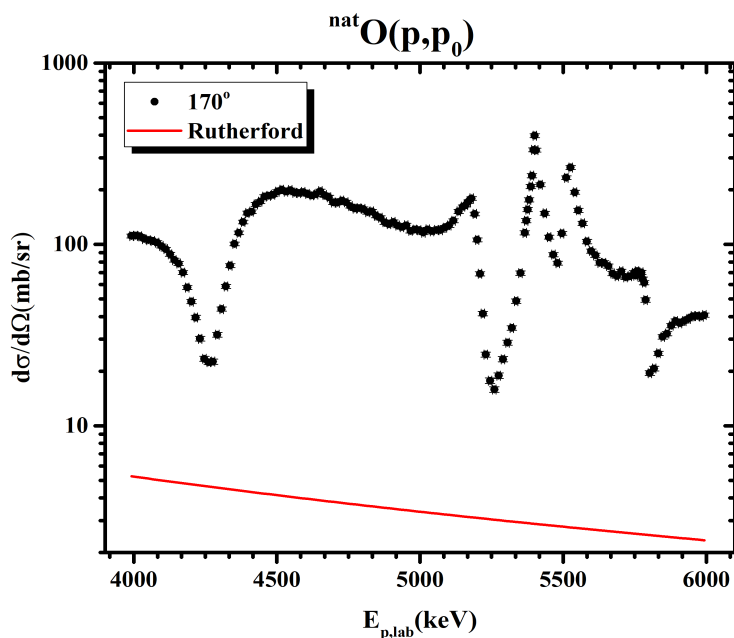
Figure 4.7: Experimental differential cross sections of the elastic backscattering of protons from ^{nat}O of the present work (black dots) along with the Rutherford formula cross section values (solid red line) for the detection angle $\theta = 170^o$ plotted in logarithmic scale.
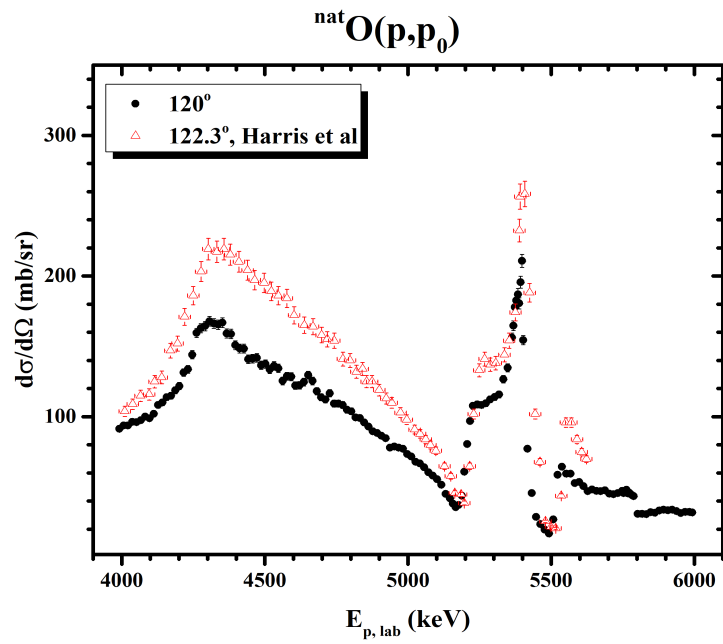
Figure 4.8: Experimental differential cross sections of the elastic backscattering of protons from ^{nat}O of the present work (black dots) for the detection angle $\theta = 120^o$ plotted with the ones from Harris et al for the detection angle $\theta = 122.3^o$ (open red triangles).
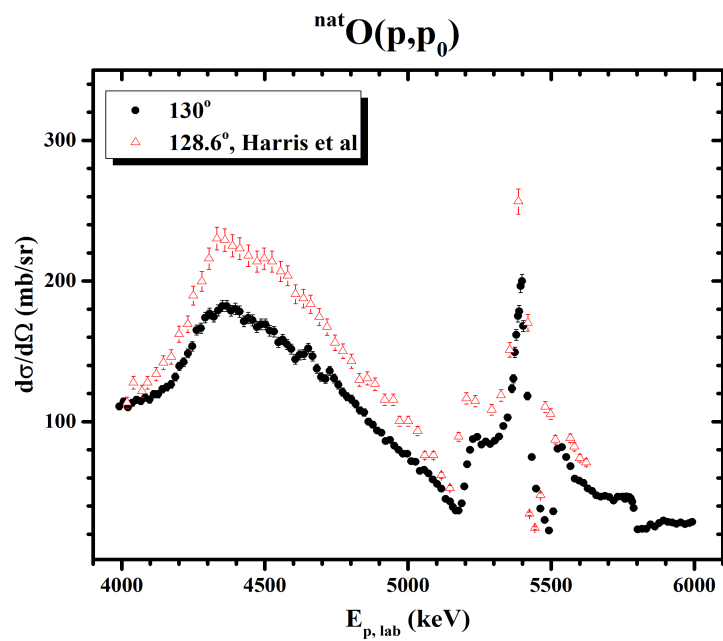
Figure 4.9: Experimental differential cross sections of the elastic backscattering of protons from ^{nat}O of the present work (black dots) for the detection angle $\theta = 130^o$ plotted with the ones from Harris et al for the detection angle $\theta = 128.6^o$ (open red triangles).
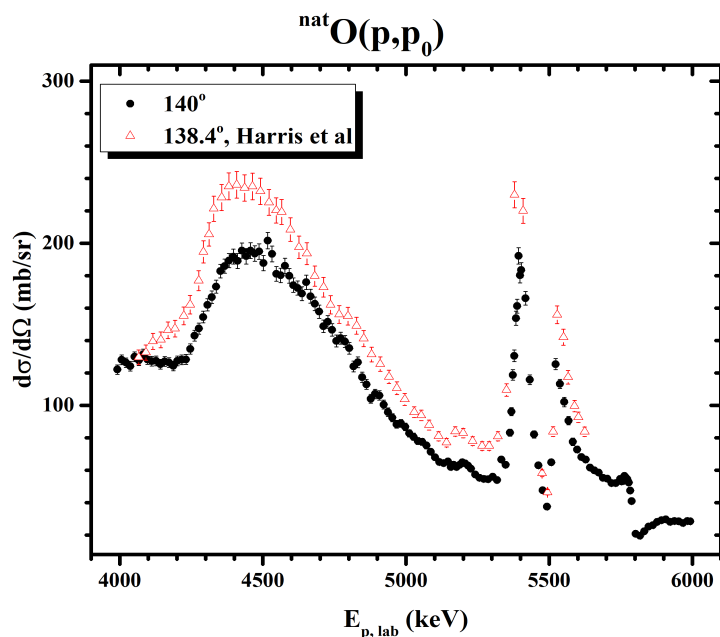
Figure 4.10: Experimental differential cross sections of the elastic backscattering of protons from ^{nat}O of the present work (black dots) for the detection angle $\theta = 140^o$ plotted with the ones from Harris et al for the detection angle $\theta = 138.4^o$ (open red triangles).
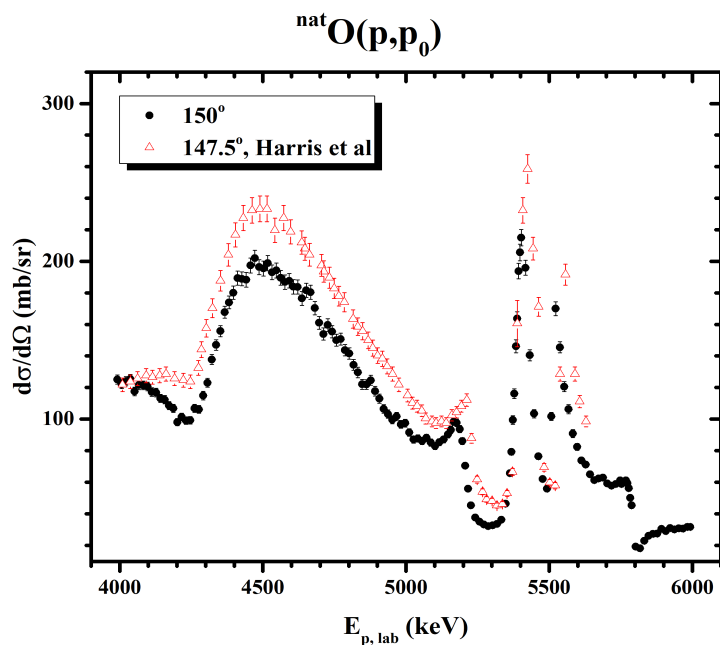
Figure 4.11: Experimental differential cross sections of the elastic backscattering of protons from ^{nat}O of the present work (black dots) for the detection angle $\theta = 150^o$ plotted with the ones from Harris et al for the detection angle $\theta = 147.5^o$ (open red triangles).
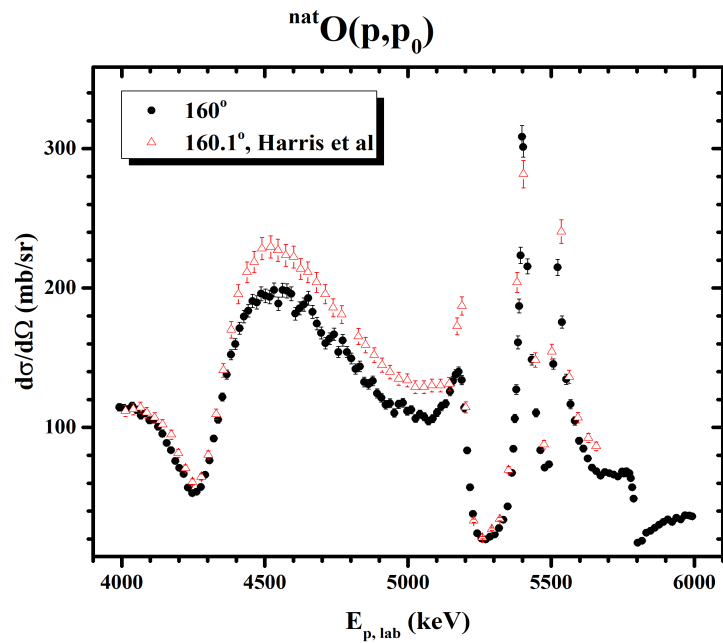
Figure 4.12: Experimental differential cross sections of the elastic backscattering of protons from ^{nat}O of the present work (black dots) for the detection angle $\theta = 160^o$ plotted with the ones from Harris et al for the detection angle $\theta = 160.1^o$ (open red triangles).
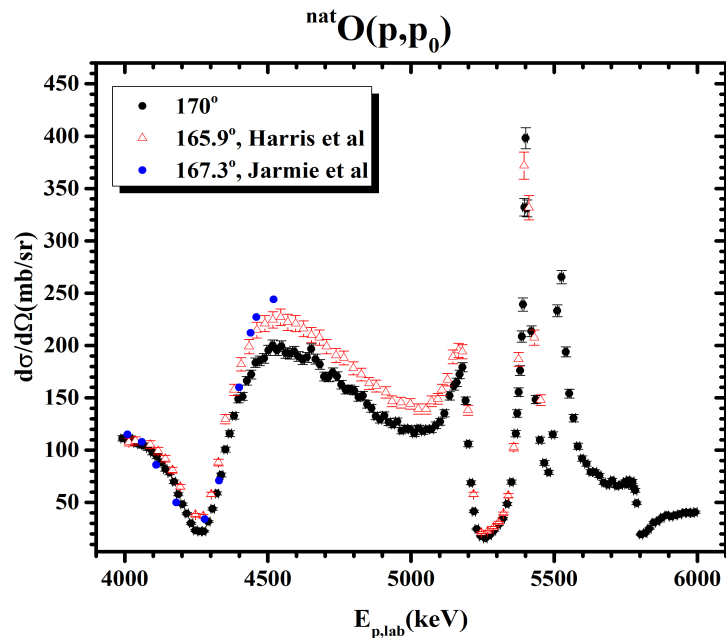
Figure 4.13: Experimental differential cross sections of the elastic backscattering of protons from ^{nat}O of the present work (black dots) for the detection angle $\theta = 170^o$ plotted with the ones from Harris et al for the detection angle $\theta = 165.9^o$ (open red triangles) and Jarmie et al for the detection angle $\theta = 167.3$(blue dots)

| $E_{p,lab}$(kev)	δE_p(kev)	$\sigma \pm \delta\sigma$ (mb/sr)									
		120°		130°		140°		150°		160°	
3992	6	91.5	1.9	110.9	2.5	122	3	125	3	114	3
4007	6	93.7	2.0	114	3	128	3	122	3	114	3
4022	6	93.7	2.0	110.3	2.4	126	3	124	3	113	3
4037	6	96.3	2.0	113	3	124	3	125	3	115	3
4052	6	96.2	2.0	116	3	130	3	117	3	113	3
4067	6	97.5	2.0	115	3	128	3	122	3	109	3
4082	6	100.0	2.1	117	3	132	3	121	3	110	3
4097	6	98.8	2.1	116	3	128	3	121	3	105	3
4112	6	102.0	2.1	120	3	127	3	117	3	106	3
4127	6	108.3	2.3	120	3	127	3	117	3	100.5	2.4
4142	6	110.1	2.3	123	3	125	3	113	3	95.4	2.3
4157	6	113.9	2.4	125	3	127	3	112	3	88.8	2.2
4172	6	114.9	2.4	126	3	126	3	108	3	83.7	2.1
4187	6	118.7	2.5	132	3	124	3	107	3	75.9	1.9
4202	6	122	3	139	3	127	3	98.1	2.3	70.9	1.8
4217	6	131	3	142	3	128	3	101.3	2.4	66.6	1.7
4232	6	134	3	149	3	128	3	99.1	2.3	56.8	1.5
4247	6	144	3	154	3	135	3	99.2	2.3	52.9	1.4
4262	6	160	3	165	4	143	3	107	3	53.7	1.4
4277	6	163	3	166	4	147	3	106.1	2.5	57.3	1.5
4292	6	164	3	174	4	155	4	115	3	65.9	1.7
4307	6	168	3	177	4	162	4	123	3	76.3	1.9
4322	6	166	3	175	4	167	4	138	3	92.1	2.3
4337	6	165	3	179	4	173	4	147	3	106	3
4352	6	167	3	182	4	183	4	156	4	122	3
4367	6	159	3	182	4	186	4	168	4	138	3
4382	6	159	3	179	4	189	4	174	4	152	4
4397	6	151	3	180	4	192	5	180	4	160	4
4412	6	148	3	178	4	189	5	189	4	171	4
4427	6	148	3	171	4	196	5	189	4	179	4
4442	6	141	3	174	4	192	5	188	5	184	5
4457	6	141	3	172	4	196	5	197	5	191	5
4472	6	142	3	167	4	194	5	202	5	190	5
4487	6	137	3	169	4	195	5	196	5	196	5
4502	6	137	3	169	4	188	5	195	5	194	5
4517	6	134	3	165	4	202	5	199	5	194	5
4532	6	136	3	164	4	193	5	193	5	199	5

$E_{p,lab}$(kev)	δE_p(kev)	$\sigma \pm \delta\sigma$ (mb/sr)									
		120°		130°		140°		150°		160°	
4547	6	134	3	156	4	181	5	194	5	189	5
4562	6	125	3	158	4	180	4	190	5	199	5
4577	6	129	3	155	4	186	5	187	5	198	5
4592	6	128	3	152	4	180	5	188	5	196	5
4607	6	122	3	144	3	174	4	184	4	182	5
4622	6	122	3	147	3	172	4	184	5	185	5
4637	6	125	3	148	3	169	4	176	4	188	5
4652	6	130	3	152	4	176	4	182	4	193	5
4667	6	125	3	147	3	167	4	180	4	183	5
4682	6	118	3	138	3	163	4	170	4	175	4
4697	6	114	3	132	3	158	4	161	4	168	4
4712	6	112.2	2.5	130	3	149	4	154	4	160	4
4727	6	117	3	136	3	151	4	160	4	164	4
4742	6	109.3	2.4	131	3	147	4	155	4	167	4
4757	6	109.4	2.4	126	3	140	4	150	4	154	4
4772	6	108.4	2.4	121	3	141	4	151	4	162	4
4787	6	104.9	2.3	118	3	139	4	144	4	154	4
4802	6	103.9	2.3	116	3	135	4	142	4	149	4
4817	6	99.6	2.2	113	3	124	3	134	3	142	4
4832	6	99.1	2.2	108	3	127	3	130	3	144	4
4847	6	95.8	2.2	107	3	117	3	122	3	133	4
4862	6	93.0	2.1	100.1	2.5	113	3	122	3	131	3
4877	6	89.6	2.0	97.9	2.4	104	3	125	3	133	4
4892	6	88.4	2.0	93.7	2.3	107	3	118	3	124	3
4907	6	86.5	2.0	92.2	2.3	106	3	113	3	121	3
4922	6	84.6	1.9	86.2	2.1	101	3	106	3	116	3
4937	6	78.1	1.8	87.1	2.2	96	3	103	3	117	3
4952	6	78.7	1.8	82.9	2.1	92.5	2.5	100	3	110	3
4967	6	78.0	1.8	79.9	2.0	88.4	2.4	102	3	117	3
4982	6	77.3	1.7	77.2	1.9	89.0	2.4	96.7	2.5	118	3
4997	6	73.4	1.7	77.2	1.9	86.8	2.3	97.5	2.5	112	3
5012	6	71.7	1.6	71.8	1.8	82.8	2.2	91.5	2.4	113	3
5027	6	67.9	1.6	71.6	1.8	80.6	2.2	87.1	2.3	106	3
5042	6	66.8	1.5	65.1	1.6	78.1	2.1	87.7	2.3	109	3
5057	6	64.1	1.5	65.9	1.7	77.6	2.1	86.1	2.2	108	3
5072	6	60.4	1.4	63.2	1.6	75.3	2.1	88.1	2.3	105	3
5087	6	58.1	1.4	58.9	1.5	71.4	2.0	85.1	2.2	106	3

$E_{p,lab}$(kev)	δE_p(kev)	$\sigma \pm \delta\sigma$ (mb/sr)									
		120°		130°		140°		150°		160°	
5102	6	55.5	1.3	55.8	1.5	68.0	1.9	83.0	2.2	111	3
5117	6	51.6	1.2	52.4	1.4	65.1	1.8	85.4	2.2	115	3
5132	6	45.1	1.0	45.0	1.2	64.3	1.7	87.1	2.2	117	3
5147	6	41.9	1.0	43.4	1.1	65.5	1.7	90.3	2.2	126	3
5157	6	38.2	0.9	39.4	1.0	61.9	1.7	93.1	2.3	133	3
5167	6	35.6	0.9	36.9	1.0	63.4	1.7	98.5	2.4	138	3
5177	6	37.2	0.9	36.8	1.0	62.0	1.7	97.6	2.4	140	3
5188	6	43.9	1.0	41.9	1.1	63.3	1.7	93.7	2.3	134	3
5197	6	60.8	1.4	53.9	1.3	64.9	1.7	86.1	2.2	114	3
5207	6	80.6	1.8	69.7	1.7	64.3	1.7	70.4	1.8	83.4	2.2
5217	6	96.9	2.1	79.9	1.9	62.8	1.7	55.9	1.5	57.0	1.5
5227	6	107.7	2.3	87.6	2.1	61.0	1.6	45.3	1.2	38.0	1.1
5242	6	108.7	2.3	89.1	2.1	57.4	1.6	37.6	1.1	24.0	0.8
5257	6	108.4	2.3	83.7	2.0	55.4	1.5	34.9	1.0	20.3	0.7
5272	6	109.5	2.3	85.8	2.0	54.6	1.5	33.2	1.0	19.6	0.7
5287	6	112.3	2.4	84.1	2.0	54.5	1.5	32.1	0.9	21.6	0.7
5303	6	114.0	2.4	86.4	2.0	55.9	1.5	32.6	0.9	23.3	0.8
5318	6	115.7	2.4	89.4	2.1	54.0	1.5	33.5	1.0	27.9	0.9
5333	6	127	3	97.0	2.3	66.6	1.8	36.3	1.0	33.7	1.0
5348	6	135	3	103.0	2.4	63.4	1.7	46.3	1.3	43.2	1.2
5363	6	156	3	124	3	83.2	2.1	65.7	1.7	67.4	1.8
5368	6	165	3	131	3	96.1	2.4	79.3	2.0	84.6	2.2
5373	6	178	4	149	4	119	3	99	3	106	3
5378	6	183	4	162	4	131	4	116	3	127	3
5384	6	187	4	175	4	154	4	146	4	161	5
5388	6	181	4	179	4	161	4	164	4	187	5
5393	6	196	4	196	5	192	5	194	5	223	6
5398	6	211	5	200	5	180	5	206	5	309	8
5403	6	154	3	168	4	183	5	215	5	301	7
5418	6	77.1	1.7	118	3	166	4	196	5	215	5
5433	6	45.7	1.1	74.8	1.8	116	3	140	3	149	4
5448	6	28.7	0.7	52.4	1.4	82.1	2.2	103	3	110	3
5463	6	23.5	0.6	38.2	1.0	63.0	1.8	76.4	2.0	83.7	2.2
5478	6	19.7	0.5	30.1	0.8	47.7	1.3	62.0	1.6	71.2	1.8
5493	6	17.0	0.4	22.6	0.6	37.6	1.0	55.8	1.4	73.5	1.8
5508	6	27.0	0.7	36.2	1.0	64.8	1.8	102	3	145	4
5523	6	58.8	1.4	80.8	2.1	125.4	3.4	170	4	215	6
5538	6	64.4	1.4	81.9	1.9	113.3	2.9	146	4	176	4

$E_{p,lab}$(kev)	δE_p(kev)	$\sigma \pm \delta\sigma$ (mb/sr)									
		120°		130°		140°		150°		160°	
5553	6	59.4	1.4	74.9	2.0	102.1	2.9	121	3	135	4
5568	6	59.4	1.4	68.3	1.8	90.5	2.6	106	3	117	3
5583	6	52.7	1.3	59.5	1.6	77.6	2.3	91	3	105	3
5598	6	53.6	1.3	58.1	1.5	72.8	2.0	82.4	2.2	90	3
5613	6	50.7	1.2	56.5	1.5	68.1	1.9	73.8	2.0	84.8	2.3
5628	6	47.0	1.1	52.7	1.4	66.5	1.9	71.2	1.9	77.7	2.2
5643	6	48.3	1.2	50.9	1.4	61.6	1.8	64.9	1.8	71.1	2.0
5658	6	47.3	1.1	47.7	1.2	60.0	1.7	61.4	1.6	68.5	1.9
5673	6	47.0	1.1	46.7	1.2	58.6	1.6	62.4	1.7	65.4	1.8
5688	6	47.6	1.1	47.3	1.2	55.4	1.5	62.9	1.7	68.0	1.9
5703	6	45.3	1.1	46.4	1.2	54.7	1.5	59.2	1.6	67.2	1.8
5718	6	44.8	1.0	43.8	1.1	52.1	1.5	57.7	1.6	66.3	1.8
5733	6	45.8	1.1	46.7	1.2	52.1	1.5	58.9	1.6	64.7	1.8
5748	6	47.2	1.1	46.7	1.2	54.6	1.5	61.2	1.6	68.3	1.9
5753	6	45.8	1.1	46.6	1.2	53.0	1.5	58.8	1.6	67.0	1.8
5758	6	46.1	1.1	45.1	1.2	53.2	1.5	60.0	1.6	66.9	1.8
5763	6	48.0	1.1	46.8	1.2	56.5	1.6	60.0	1.6	68.6	1.9
5768	6	45.5	1.1	45.6	1.2	55.5	1.6	61.1	1.6	67.0	1.8
5773	6	45.8	1.1	46.4	1.2	54.4	1.5	59.5	1.6	67.2	1.8
5778	6	44.9	1.1	45.6	1.2	52.4	1.5	56.2	1.5	63.5	1.7
5783	6	44.0	1.0	43.1	1.1	47.5	1.4	50.0	1.4	57.0	1.6
5788	6	43.4	1.0	38.5	1.0	41.0	1.2	45.3	1.3	48.9	1.4
5803	6	30.9	0.7	23.4	0.6	20.7	0.6	19.1	0.6	17.2	0.6
5818	6	31.0	0.7	23.8	0.6	19.6	0.6	18.1	0.5	18.7	0.6
5833	6	30.7	0.7	23.8	0.6	22.3	0.7	22.8	0.6	24.5	0.7
5848	6	32.1	0.7	27.0	0.7	25.3	0.7	26.0	0.7	25.8	0.7
5863	6	31.8	0.7	25.4	0.7	26.1	0.7	27.1	0.7	27.9	0.8
5878	6	33.3	0.8	28.0	0.7	28.1	0.8	27.4	0.8	30.3	0.8
5893	6	33.9	0.8	29.8	0.8	29.1	0.8	30.4	0.8	32.1	0.9
5908	6	33.5	0.8	28.8	0.7	29.6	0.8	28.9	0.8	33.9	0.9
5923	6	33.8	0.8	28.4	0.7	28.2	0.8	31.0	0.8	32.3	0.9
5938	6	33.0	0.8	27.4	0.7	28.7	0.8	30.0	0.8	35.2	1.0
5953	6	31.6	0.7	28.4	0.7	28.5	0.8	30.7	0.8	34.0	0.9
5968	6	32.2	0.7	27.1	0.7	27.4	0.8	30.6	0.8	36.8	1.0
5983	6	32.4	0.7	27.9	0.7	28.7	0.8	31.7	0.8	36.8	1.0
5993	6	31.9	0.7	28.8	0.7	28.5	0.8	31.6	0.8	36.2	1.0

Table 4.1

$E_{p,lab}$(kev)	δE_p(kev)	$\sigma \pm \delta\sigma$ (mb/sr)	
		170°	
3992	6	111	3
4007	6	112	3
4022	6	111	3
4037	6	107	3
4052	6	105.7	2.5
4067	6	104.5	2.5
4082	6	102.3	2.4
4097	6	98.0	2.3
4112	6	94.1	2.3
4127	6	88.2	2.1
4142	6	81.9	2.0
4157	6	78.5	1.9
4172	6	69.9	1.7
4187	6	57.9	1.5
4202	6	48.4	1.3
4217	6	39.5	1.1
4232	6	30.2	0.9
4247	6	23.4	0.7
4262	6	22.4	0.7
4277	6	22.6	0.7
4292	6	31.8	0.9
4307	6	44.0	1.2
4322	6	58.7	1.5
4337	6	76.3	1.9
4352	6	100.7	2.4
4367	6	116	3
4382	6	133	3
4397	6	149	4
4412	6	151	4
4427	6	166	4
4442	6	172	4
4457	6	184	5
4472	6	185	5
4487	6	188	5
4502	6	195	5
4517	6	200	5
4532	6	195	5

$E_{p,lab}$(kev)	δE_p(kev)	$\sigma \pm \delta\sigma$ (mb/sr)	
		170°	
4547	6	199	5
4562	6	193	5
4577	6	192	5
4592	6	194	5
4607	6	190	5
4622	6	186	5
4637	6	189	5
4652	6	197	5
4667	6	187	5
4682	6	182	5
4697	6	170	4
4712	6	170	4
4727	6	174	4
4742	6	171	4
4757	6	163	4
4772	6	158	4
4787	6	158	4
4802	6	157	4
4817	6	151	4
4832	6	152	4
4847	6	144	4
4862	6	140	4
4877	6	133	3
4892	6	129	3
4907	6	133	3
4922	6	127	3
4937	6	125	3
4952	6	128	3
4967	6	119	3
4982	6	121	3
4997	6	120	3
5012	6	116	3
5027	6	121	3
5042	6	118	3
5057	6	120	3
5072	6	120	3
5087	6	124	3

$E_{p,lab}$(kev)	δE_p(kev)	$\sigma \pm \delta\sigma$ (mb/sr)	
		170°	
5102	6	127	3
5117	6	135	3
5135	6	152	4
5150	6	161	4
5160	6	165	4
5170	6	172	4
5180	6	179	4
5191	6	147	4
5200	6	106	3
5210	6	68.8	1.8
5220	6	41.5	1.2
5230	6	24.7	0.8
5245	6	17.7	0.6
5260	6	15.8	0.6
5275	6	18.9	0.7
5290	6	23.3	0.8
5306	6	28.7	0.9
5321	6	34.6	1.0
5336	6	48.7	1.3
5351	6	69.5	1.9
5366	6	116	3
5371	6	135	4
5376	6	155	4
5381	6	176	5
5387	6	209	5
5391	6	239	6
5396	6	332	8
5401	6	398	10
5406	6	331	8
5421	6	214	5
5436	6	148	4
5451	6	110	3
5466	6	87.7	2.2
5481	6	78.8	1.9
5496	6	115	3
5511	6	233	6
5526	6	265	6
5541	6	194	5

$E_{p,lab}$(kev)	δE_p(kev)	$\sigma \pm \delta\sigma$ (mb/sr)	
		170°	
5553	6	154	4
5568	6	131	4
5583	6	104	3
5598	6	91.9	2.5
5613	6	87.0	2.3
5628	6	79.1	2.2
5643	6	79.2	2.2
5658	6	76.0	2.0
5673	6	69.1	1.8
5688	6	66.8	1.8
5703	6	71.1	1.9
5718	6	65.9	1.8
5733	6	66.7	1.8
5748	6	69.8	1.9
5753	6	67.3	1.8
5758	6	71.2	1.9
5763	6	69.8	1.9
5768	6	68.1	1.8
5773	6	70.1	1.9
5778	6	64.3	1.7
5783	6	61.5	1.7
5788	6	49.4	1.4
5803	6	19.5	0.6
5818	6	20.7	0.6
5833	6	25.1	0.7
5848	6	30.9	0.8
5863	6	32.2	0.9
5878	6	35.7	0.9
5893	6	37.8	1.0
5908	6	36.8	1.0
5923	6	37.8	1.0
5938	6	38.9	1.0
5953	6	40.2	1.0
5968	6	40.3	1.0
5983	6	40.0	1.0
5993	6	40.8	1.0

Table 4.2

4.2 A short introduction to the R-matrix theory

The theoretical investigation of the $^{16}O(p,p_0)$ scattering has been performed in the present thesis, within the R-matrix framework. The R-matrix theory,

initially developed by Wigner and Eisenbud, originally described only the resona nces in nuclear reactions. Soon after, it became a powerful tool in parametrizing non-resonant regions of the cross sections. The most distinctive advantage of the theory is the ability to parametrize differential cross sections of low energy nuclear reactions using parameters that can be directly compared to experimentally measured quantities. So, not only are the data fitted, but the parameters themselves are connected to physical properties of the scattering states. The R-matrix theory has been developed in two separate categories, the phenomenological R-matrix and the calculable R-matrix theory. The main focus of the latter is to provide solutions to the coupled channel Schroedinger equation when there are several open channels via which a reaction can proceed. The first variant, the phenomenological R-matrix, is predominantly used in low energy nuclear reactions parametrization. A thorough and comprehensive review of this theory has been done by Lane and Tomas in 1958 [15].

4.2.1 Basic principles

The pillar of the R-matrix theory is that the configuration space is separated into two distinct regions, the internal and the external one. In the internal region, strong nuclear forces prevail, while in the external only the electromagne tic interactions appear. The two regions are separated by the so-called channel radius which is big enough, so that in the external region only the electromagnetic forces exist. The advantage of such an assumption is that the wave functions in the outer region have an analytical form (Shroedinger equation can be solved), while the wave functions of the interior can be expanded as a linear combination of the eigenfunctions X_λ of the Hamiltonian. Eigenvalues of the Hamiltonian are the energy levels of the compound nucleus. The interactions in the interior are determined by the unknown nuclear potential. A key assumption of the theory is the continuity of the wavefunctions and their derivatives at the boundary (channel radius). Typically, when a projectile of mass number A_1 hits a target with mass number A_2, channel radius is chosen as $a_c = r_0 \cdot (A_1^{1/3} + A_2^{1/3})$, where $r_0 = 1.1 - 1.4$ fm. In the following subsections 4.2.2 and 4.2.3, the physics of the internal and external region in the framework of the few- channel, multi-level R-matrix theory are discussed. In this approach , the external region is divided into the possible channels through which the compound nucleus can be formed or decay.

4.2.2 External region

The radial component of the external wave function satisfies the Schroedinger equation that includes the centrifugal and Coulomb terms and is given by (it applies only if there is only one channel available for the formation and decay of the compound nucleus):

$$\frac{d^2\varphi_\ell}{dr^2} - \left[\frac{\ell(\ell+1)}{r^2} + \frac{2m}{\hbar^2}\left(-E + \frac{Z_1 Z_2 e^2}{r}\right)\right]\varphi_\ell = 0 \tag{4.2}$$

The eq4.2 has solutions the regular F_ℓ (finite at r=0) and irregular G_ℓ (not finite at r=0) Coulomb wave functions, whose asymptotic behavior is given by:

$$F_\ell \sim \sin\left[kr - \eta\log(2kr) - \left(\frac{1}{2}\right)\ell\pi + \sigma_\ell\right]$$
$$G_\ell \sim \sin\left[kr - \eta\log(2kr) - \left(\frac{1}{2}\right)\ell\pi + \sigma_\ell\right]$$

(4.3)

where the Coulomb phase shift and parameter are given by:

$$\sigma_\ell = \arg[1 + \ell + i\eta]$$
$$\eta = Z_1 Z_2 e^2 / h\nu$$

(4.4)

The solutions for the incoming waves I_ℓ and outgoing waves O_ℓ are given with respect to F_ℓ, G_ℓ as:

$$I_\ell = (G_\ell - iF_\ell)\exp\left(i\omega_\ell\right)$$
$$O_\ell = (G_\ell + iF_\ell)\exp\left(-i\omega_\ell\right)$$

(4.5)

and $\omega_\ell = \sum_{n=1}^{\ell}\tan\left(\frac{\eta}{n}\right)$ being the Coulomb phase. From now on, the penetration factor P_ℓ, the shift function S_ℓ and the scattering phase shift Ω_ℓ for each partial wave can be defined as:

$$P_\ell = (kr)/\left(F_\ell^2 + G_\ell^2\right)$$
$$S_\ell = \left(F_\ell'F_\ell + G_\ell'G_\ell\right)/\left(F_\ell^2 + G_\ell^2\right)$$
$$\Omega_\ell = \omega_\ell - tan(F_\ell/G_\ell)$$

(4.6)

In general, the compound nucleus can be formed or decay through many channels and may include many energy levels. So, the main goal is to somehow include these extra complications in the preceding formulae. Thus, the quantities that have been defined in equations:4.6, 4.5 become all matrices. In the end the collision matrix will thus be defined, whose rows and columns pertain to channels.

We begin the description of the nuclear resonances, when retaining a few channels by writing the total external wave function as the sum of products, for each channel c, of the radial wave function φ_c, with the channel wave function Ψ_c:

$$\psi = \sum_c \Psi_c\varphi_c$$

(4.7)

So, the wave function at the surface defining the boundary between the internal and the external region can be expanded in terms of channels. Each channel is assigned with a pair of good quantum number such as the channel spin s, the relative angular momentum ℓ between the projectile and the target and an additional subscript a, which denotes the pair of particles each time. From now on, $c = asl$ is the collective quantum number. Finally,the external part of the radial component of the wave function for each channel c, is given by :

$$\phi_c = \left(\frac{1}{v_c}\right)^{\frac{1}{2}}(y_c I_c + x_c O_c)$$

(4.8)

where I_c, O_c are the incoming and outgoing wave functions which can be calculated from the regular and the irregular Coulomb functions F_c and G_c respectively, y_c and x_c are the amplitudes of the incoming and outgoing waves respectively and v_c the relative channel velocity. The amplitudes y_c and x_c of the incoming and outgoing waves are related via the collision matrix $U_{cc'}$ as:

$$x_c = -\sum_{c'} U_{cc'} y_{c'} \tag{4.9}$$

So, the final expression for the radial component of the external wave function for each channel is given by:

$$\phi_c = \left(\frac{1}{v_c}\right)^{\frac{1}{2}} \left(y_c I_c - \sum_{c'} U_{cc'} y_{c'} O_{c'} \right) \tag{4.10}$$

4.2.3 Internal region

In the internal region, the resonant states X_ℓ of the compound nucleus are the eigenfunctions of the Hamiltonian:

$$HX_\lambda = E_\lambda X_\lambda \tag{4.11}$$

with the imposed boundary condition for each channel c:

$$[(r_c dX_\lambda/dr_c)/X_\lambda]_{r_c = a_c} = b_c \tag{4.12}$$

Also, in the full configuration space, the Schroedinger equation for the full wave function is also given by:

$$H\Psi = E\Psi \tag{4.13}$$

The resonant states form a complete set, so the total wave function Ψ can be expanded as:

$$\Psi = \sum_\lambda C_\lambda X_\lambda \tag{4.14}$$

where the coefficients C_λ are calculated via:

$$C_\lambda = \int_V \Psi X_\lambda^* dV \tag{4.15}$$

where V is the total volume of the compound nucleus. Multiplying 4.13 with X_λ^* and the complex conjugate of 4.11 with Ψ, we subtract and integrate over the whole nuclear volume V, to calculate C_λ:

$$C_\lambda = (E_\lambda - E)^{-1} \sum_c \gamma_{\lambda c}(\phi_c' - b_c \phi_c)(\hbar^2/2m_c r_c)^{1/2} \tag{4.16}$$

Plugging 4.16 into 4.14 and evaluating 4.14 on the channel surface S, the radial component of the wave function of an internal channel c is given by [23]:

$$\phi_c = \left(\frac{m_c r_c}{\hbar^2}\right)^{\frac{1}{2}} \sum_{c'} R_{cc'} \left(\frac{\hbar^2}{m_{c'} r_{c'}}\right)^{\frac{1}{2}} [\phi_{c'}' - b_{c'} \phi_{c'}] \tag{4.17}$$

where m_c is the reduced mass, r_c is the channel radius and the prime denotes the derivative with respect to $r_c d/dr_c$. The b_c is the boundary condition that the logarithmic derivative of the eigenstate X_λ has to satisfy at the channel radius. Also, equation 4.17 introduces the R-matrix which contains all the information regarding the compound nucleus system [5]:

$$R_{cc'} = \sum_\lambda \frac{\gamma_{\lambda c}\gamma_{\lambda c'}}{E_\lambda - E} \tag{4.18}$$

where

$$\gamma_{\lambda c} = \left(\frac{\hbar^2}{2m_c a_c}\right)^{\frac{1}{2}} \int dS X_\lambda^* \psi_c$$

are the reduced widths. Basically, $\gamma_{\lambda c}$ expresses the overlap of the eigenstates X_λ with the channel wave function Ψ_c. In other words, it is the measure of the contribution of the level λ of the compound nucleus to the wave function of the channel c.

Finally, matching the logarithmic derivatives of the radial components of the wave functions of the internal and the external region (see eq4.10, 4.17) on the channel surface r_c, we get the collision matrix in terms of the R-matrix:

$$U_{cc'} = (k_c r_c)^{1/2} O_c^{-1} \sum_{c''} [1 - RL]_{c''}^{-1} [\delta_{c''} - R_{c''c'} L_{c'}^*] I_{c'} (k_{c'} r_{c'})^{-1/2} \tag{4.19}$$

where k_c is the wavenumber of channel c, $O_c, O_c^{-1}, (k_c r_c)^{1/2}, (k_c r_c)^{-1/2}$ are the diagonal elements of the diagonal matrices $O, O^{-1}, (kr)^{1/2}, (kr)^{-1/2}$ respectively [22]. Finally, L_c are the diagonal elements of the diagonal matrix L, which are given by:

$$L_c = O_c' O_c^{-1} - b_c = S_c + iP_c \tag{4.20}$$

where S_c, P_c are the shift function and the penetrability factor for each channel.

4.3 AZURE software

To perform the theoretical calculations, the AZURE software has been used. AZURE is a multichannel, multilevel R-matrix computer code in which low energy nuclear reactions, involving charged particles, gamma rays and neutrons, can be modeled and extrapolated to low energies relevant to nuclear astrophysics. It allows for the computation of level energies (along with the corresponding J^π), partial observed widths and bound state normalization parameters.

In our case, elastic scattering differential cross sections of protons from ^{nat}O have been computed theoretically in the energy range $E = 600 - 6000$ keV for $\theta = 140^o - 170^o$. The existing evaluation for oxygen that is available in IBANDL up to 4080 keV has been theoretically reproduced. To perform the corresponding calculations the (reaction) channel radius has to be specified. In this study the channel radius was chosen to be $a = 3.057$ fm. It should be noted that the calculations were sensitive to the choice of the channel radius, and the aforementioned value was deemed as the most suitable to fit the data. The next step is to determine the exit channels of the reaction as well as the

masses, the spins and parities of the reacting nuclei (namely $^{16}O, ^{13}N, ^{4}He$ and p). Afterwards, the energy levels of the compound nucleus have to be completed. So, for each level of the compound nucleus ^{17}F the energy and the J^π were set. The code also automatically computes the channels through which a particular level can decay according to the conservation of angular momentum and parity. The maximum relative angular momentum that contributed to the formation of the compound nucleus was $\ell = 3$. After each energy level is specified, the user has to determine a partial width Γ, also referred as observed width, for each decaying channel, namely the proton and alpha particle width. A set of initial values for the energies E_λ and observed widths was assigned for each level of the compound nucleus. The code allows for some parameters to be fixed and others to be fitted. The only free parameters were the energy and the partial widths of the resonances at $E_x = 4640, 5000, 6037$ keV along with the energy and partial width of virtual resonance at $E_x = 6917.9$ keV.

As mentioned above, a virtual resonance at $E_x = 6917.9$ keV with a width $\Gamma_p = 2.65595 \cdot 10^6$ eV had to be included in our calculations to fit the high energy region of the cross section (5.8-6 MeV). In this energy range, contributions from the direct reaction mechanism may affect the structure of the cross section, which the AZURE code does not take into account. Another interesting thing to consider is the contribution of hard sphere external capture components in the cross section. This is parametrized by the Asymptotic Normalization Coefficient (ANC) of the ground state ($J^\pi = 5/2^+$) and the first excited state with $J^\pi = 1/2^+$. These coefficients can be experimentally deduced. In fact, previous measurements by Gagliardi et al [11] and Iliadis et al [13] have found ANC's values of $C = 1.04 \pm 0.05 fm^{-1/2}$ and $C = 1.13 \pm 0.01 fm^{-1/2}$ for the ground state respectively, and $C = 80.6 \pm 4.2 fm^{-1/2}$ and $C = 82.3 \pm 0.3 fm^{-1/2}$ for the first excited state. Our values of $1.03 fm^{-1/2}$ and 76.1 fm$^{-1/2}$ differ by 6% from Gagliardi for the first excited state, while are in perfect agreement for the ground state and by 8% and 9.7% from Iliadis for the first excited and ground state respectively. The adopted values fit the evaluated data as it can be seen from fig. 4.14-4.17. A major discrepancy with the literature is observed at the width of the resonance at $E_x = 5804$ keV. While a value of $\Gamma = 59000$ eV is obtained from R-matrix calculations, the experimental value is $\Gamma = 180000$ eV, which is an underestimation by a factor of three. Finally, the detection angles $\theta = 120^o$ and $\theta = 130^o$ were excluded from the calculations since no satisfactory convergence to the data could be achieved. Theoretical calculations overestimated the cross sections up to 35% on the resonance at $E_x = 5$ MeV. A possible explanation would be that oxygen and nitrogen peaks do not separate at this geometry and so the integration of the peaks underestimates the cross section. Therefore, systematic errors from the integration and the background determination may be the source of the discrepancies.

The resulting theoretical curve at the detection angle $\theta = 140^o$ overestimates the experimental cross section by up to 15% in the energy range $E_{p,lab} = 4100 - 5150$ keV and by 26% the maximum of the resonance peak at $E_{p,lab} = 5403$ keV. Also, theoretical calculations underestimate cross section values up to 21% in the energy range $E_{p,lab} = 4650 - 5100$ keV and by 20% the peak of the resonance at $E_{p,lab} = 5403$ keV at $\theta = 170^o$. Finally, the R-matrix calculations are in fair

agreement with the experimental points at the detection angles $\theta = 150^o, 160^o$ over the whole energy range.

On table 4.3 the parameters that modeled the differential cross sections were tabulated. Despite the fact that the resonances at $E_x = 6697$keV and $E_x = 6774$keV are not energetically accessible, they were included in the calculations to better reproduce the non resonant region of the cross section. Even though evaluated data come without error bars, an error of 3% was assigned at each point in the energy range $E = 600 - 3980$ keV to allow the code to perform the fit.

Energy (keV)	J^π	Γ_p (eV)	Γ_a (eV)	ANC (fm$^{-1/2}$)	$\Gamma_{literature}$ (eV)
0	$5/2^+$	-	-	1.03	-
495.3	$1/2^+$	-	-	76.1	-
3106.3	$1/2^-$	17700	0	-	19000
3864,69	$5/2^-$	1500	0	-	1500
4617.7	$3/2^-$	225000	0	-	225000
4922.6	$3/2^+$	$1.73 \cdot 10^6$	0	-	$1.53 \cdot 10^6$
5486	$3/2^-$	55000	8500	-	68000
5681	$7/2^-$	36000	6000	-	40000
5804	$3/2^+$	59000	0	-	180000
6052	$1/2^-$	21000	12000	-	30000
6697	$5/2^+$	1500	0	-	1500
6774	$3/2^+$	4500	0	-	4500
6917.9	$1/2^+$	$2.65595 \cdot 10^6$	0	-	-

Table 4.3: Best fit parameters implemented in the AZURE code for the reaction $p + {}^{16}O$, with a channel radius $a_c = 3.057$ fm. Also, the values of the total width of each resonance found at [1] is tabulated for comparison with the ones of the present work. In all cases total widthσ correspond only to proton widths.
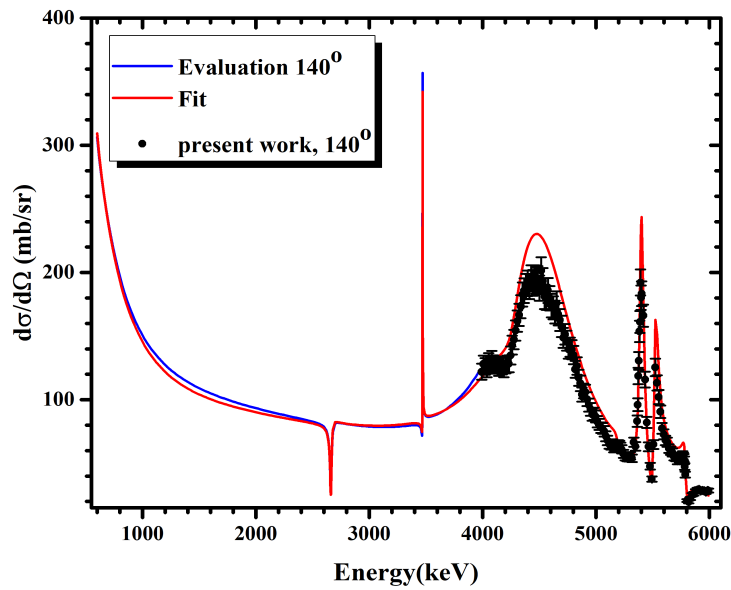
Figure 4.14: Current evaluation present in the IBANDL up to proton beam energy $E = 3980$ keV (solid blue line) is plotted in the same graph with the experimental data points (black dots) and the AZURE fit in the energy range $E = 600 - 6000$ keV (solid red line) for the detection angle $\theta = 140^o$.
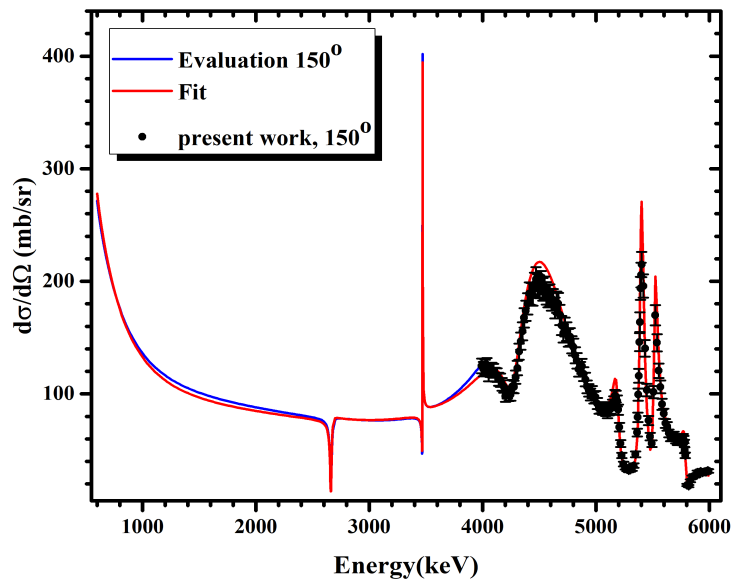

Figure 4.15: Current evaluation present in the IBANDL up to proton beam energy $E = 3980$ keV (solid blue line) is plotted in the same graph with the experimental data points (black dots) and the AZURE fit in the energy range $E = 600 - 6000$ keV (solid red line) for the detection angle $\theta = 150^o$.

Figure 4.16: Current evaluation present in the IBANDL up to proton beam energy $E = 3980$ keV (solid blue line) is plotted in the same graph with the experimental data points (black dots) and the AZURE fit in the energy range $E = 600 - 6000$ keV (solid red line) for the detection angle $\theta = 160^o$.
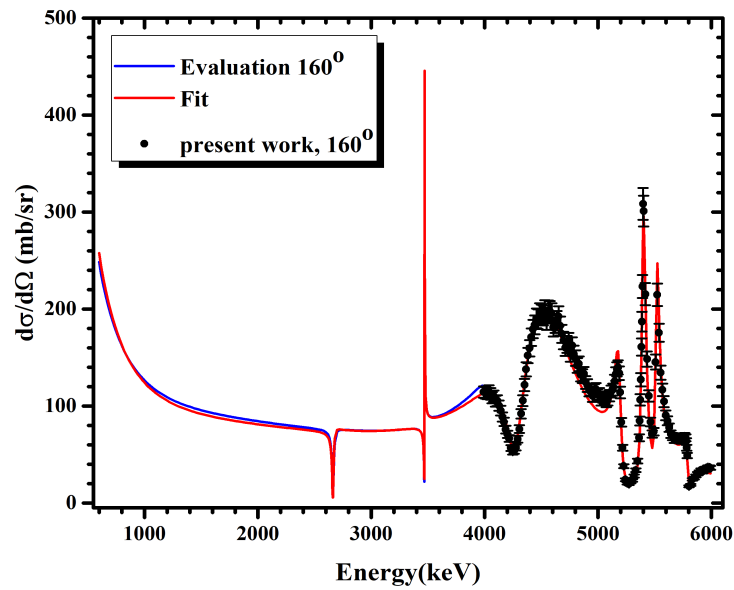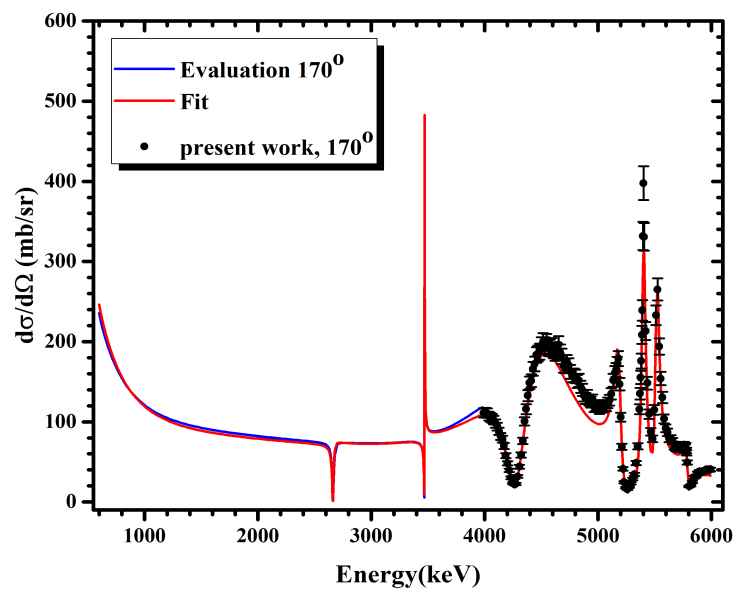

Figure 4.17: Current evaluation present in the IBANDL up to proton beam energy $E = 3980$ keV (solid blue line) is plotted in the same graph with the experimental data points (black dots) and the AZURE fit in the energy range $E = 600 - 6000$ keV (solid red line) for the detection angle $\theta = 170^o$.

Chapter 5

Conclusions and future perspectives

In the present work, the elastic backscattering differential cross sections of protons from ^{nat}O have been measured in the energy range $E = 4 - 6$ MeV at six backscattering angles $\theta = 120^o - 170^o$ with a step of 10°. The measurements were conducted at the 5.5 MV Tandem Van De Graaff accelerator at the Institute of Nuclear and Particle Physics of N.C.S.R. 'Demokritos'. The energy step varied from 5-15 keV. The smaller energy step was adopted to study the structure of the narrow resonances present in the ^{17}F compound nucleus levels.

The cross section structure exhibits six resonances which come from the energy levels of the compound nucleus ^{17}F. Their shape and angular dependence is determined from the corresponding J^π, the total width and potential overlapping with neighboring resonances. Also, strong deviations from the Rutherford cross section formula have been observed, which reach up to a factor of 138 times higher.

Also, the structure of the cross section is predominantly affected from the giant resonance at $E_x =$ 5 MeV ($\Gamma = 1.53$ MeV). Due to its width it interferes with the neighboring narrow resonances thus affecting their shape and amplitude. Moreover, more experimental data points have been collected in the energy range $E = 5140 - 5600$ keV to probe the structure of the cross section, where three narrow resonances of the ^{17}F compound nucleus at $E_x = 5488, 5672, 5820$ keV are present. Also, the measurements of the present work enriched the current literature with never measured before data in the energy range E= 5.6- 6 MeV at six backscattering angles $120^o - 170^o$. Finally, the coherent set of data created may serve for the future expansion of the current evaluation up to 6 MeV proton lab energy.

The theoretical investigation of the experimental cross sections has been performed using the AZURE code for the detection angles $\theta = 140^o - 170^o$ in the energy range $E = 600 - 6000$ keV . For that purpose R-matrix calculations have been performed to fit the experimental data points. The set of parameters used, fitted the current evaluation in the energy range $E = 600 - 3980$ keV and the experimental data of the present work with great accuracy. However, discrepancies are observed in the energy range $E = 4100 - 5150$ keV for the detection angle $\theta = 140^o$ and in the energy range $E_{p,lab} = 4650 - 5100$ keV for

the detection angle $\theta = 170^o$ and at the peak of the resonance around the proton lab energy $E_{p,lab} = 5400$ keV. Additionally, the theoretical reproduction of the differential cross sections for the detection angles $120^o, 130^o$ was not possible with the current set of parameters used.

For that reason, a more rigorous investigation of the theoretical results should be conducted to mitigate the discrepancies between the data and theoretical results. From the experimental point of view, it is crucial that benchmarking experiments are conducted from independent laboratories to cross validate the differential cross sections of the present work. Hopefully, the discrepancies between the previous measurements and the results of the present work will thus be resolved.

Bibliography

[1] National nuclear data center. https://www.nndc.bnl.gov/.

[2] NCSR Tandem, accelerator description. http://tandem.inp.demokritos.gr/t_accel_description.html, 2010.

[3] F. Abel, G. Amsel, E. d'Artemare, C. Ortega, J. Siejka, and G. Vizkelethy. Use of the 16o(3he, α)15o reaction for studying oxygen-containing thin films. *Nuclear Instruments and Methods in Physics Research Section B: Beam Interactions with Materials and Atoms*, 45(1):100–104, 1990.

[4] W. Assmann, H. Huber, C. Steinhausen, M. Dobler, H. Glückler, and A. Weidinger. Elastic recoil detection analysis with heavy ions. *Nuclear Instruments and Methods in Physics Research Section B: Beam Interactions with Materials and Atoms*, 89(1):131–139, 1994.

[5] R. Azuma, E. Uberseder, E. Simpson, C. Brune, H. Costantini, R. Deboer, J. Görres, M. Heil, P. Leblanc, C. Ugalde, and M. Wiescher. Azure: An r-matrix code for nuclear astrophysics. *Physical Review C - PHYS REV C*, 81, 04 2010.

[6] J. Biersack and J. Ziegler. Refined universal potentials in atomic collisions. *Nuclear Instruments and Methods in Physics Research*, 194(1):93–100, 1982.

[7] B. Blanpain, P. Revesz, L. Doolittle, K. Purser, and J. Mayer. The use of the 3.05 mev oxygen resonance for 4he backscattering near-surface analysis of oxygen-containing high z compounds. *Nuclear Instruments and Methods in Physics Research Section B: Beam Interactions with Materials and Atoms*, 34(4):459–464, 1988.

[8] W. Catford. Catkin, v. 2.01 c the relativistic kinematics program. Technical report, Technical report, 2004.

[9] W. K. Chu. Calculation of energy straggling for protons and helium ions. *Phys. Rev. A*, 13:2057–2060, Jun 1976.

[10] D. D. Cohen and E. K. Rose. Analysis of oxygen by charged particle bombardment. *Nuclear Instruments and Methods in Physics Research Section B: Beam Interactions with Materials and Atoms*, 66(1):158–190, 1992.

[11] C. A. Gagliardi, R. E. Tribble, A. Azhari, H. L. Clark, Y.-W. Lui, A. M. Mukhamedzhanov, A. Sattarov, L. Trache, V. Burjan, J. Cejpek, V. Kroha,

i. c. v. Piskoř, and J. Vincour. Tests of transfer reaction determinations of astrophysical s factors. *Phys. Rev. C*, 59:1149–1153, Feb 1999.

[12] R. Harris, G. Phillips, and C. Miller Jones. Phase shift analysis of the elastic scattering of protons from oxygen. *Nuclear Physics*, 38:259–280, 1962.

[13] C. Iliadis, C. Angulo, P. Descouvemont, M. Lugaro, and P. Mohr. New reaction rate for $^{16}O(p,\gamma)^{17}F$ and its influence on the oxygen isotopic ratios in massive agb stars. *Phys. Rev. C*, 77:045802, Apr 2008.

[14] N. Jarmie and J. Seagrave. Los alamos scientific lab. *LA-2014*, 1957.

[15] A. M. Lane and R. G. Thomas. R-matrix theory of nuclear reactions. *Rev. Mod. Phys.*, 30:257–353, Apr 1958.

[16] J. L'ecuyer, J. Davies, and N. Matsunami. How accurate are absolute rutherford backscattering yields. *Nuclear Instruments and Methods*, 160(2):337–346, 1979.

[17] M. Mayer. Improved physics in simnra 7. *Nuclear Instruments and Methods in Physics Research Section B: Beam Interactions with Materials and Atoms*, 332:176–180, 2014. 21st International Conference on Ion Beam Analysis.

[18] H. Rafi-kheiri, O. Kakuee, and M. Lamehi-Rachti. Differential cross section measurement of 16o(d,p0,1) reactions at energies and angles relevant to nra. *Nuclear Instruments and Methods in Physics Research Section B: Beam Interactions with Materials and Atoms*, 371:46–49, 2016. The 22nd International Conference on Ion Beam Analysis (IBA 2015).

[19] C. E. Rolfs and W. S. Rodney. *Cauldrons in the cosmos: Nuclear astrophysics*. University of Chicago press, 1988.

[20] J. Theuerkauf, S. Esser, S. Krink, M. Luig, N. Nicolay, O. Stuch, and H. Wolters. Tv analysis code. *University of Cologne*, 2000.

[21] A. Turos, L. Wieluński, and A. Barcz. Use of the nuclear reaction 16o(d,α)14n in the microanalysis of oxide surface layers. *Nuclear Instruments and Methods*, 111(3):605–610, 1973.

[22] E. Vogt. Theory of low energy nuclear reactions. *Reviews of Modern Physics*, 34(4):723, 1962.

[23] E. W. Vogt. R-matrix theory*. 2005.

[24] Q. Yang, D. O'Connor, and Z. Wang. Empirical formulae for energy loss straggling of ions in matter. *Nuclear Instruments and Methods in Physics Research Section B: Beam Interactions with Materials and Atoms*, 61(2):149–155, 1991.